Anguilliform and carangiform fish-inspired hydrodynamic study for an undulating hydrofoil: Effect of shape and adaptive kinematics

Siddharth Gupta
Department of Mechanical Engineering, Indian Institute of Technology Bombay, Mumbai 400076, India; Fluids Laboratory for Aeronautical and Industrial Research (FLAIR), Department of Mechanical and Aerospace Engineering, Monash University, Melbourne, Victoria 3800, Australia; and IITB-Monash Research Academy, IIT Bombay, Mumbai 400076, India

Amit Agrawal
Department of Mechanical Engineering, Indian Institute of Technology Bombay, Mumbai 400076, India

Kerry Hourigan
Fluids Laboratory for Aeronautical and Industrial Research (FLAIR), Department of Mechanical and Aerospace Engineering, Monash University, Melbourne, Victoria 3800, Australia

Mark C. Thompson
Fluids Laboratory for Aeronautical and Industrial Research (FLAIR), Department of Mechanical and Aerospace Engineering, Monash University, Melbourne, Victoria 3800, Australia

Atul Sharma*
Department of Mechanical Engineering, Indian Institute of Technology Bombay, Mumbai 400076, India

(Received 27 November 2021; accepted 24 August 2022; published 14 September 2022)

Anguilliform and carangiform fish have a thinner and thicker body along with a smaller and larger undulating wavelength-based kinematics for their propulsion, respectively. The present work is motivated by the fact that both types of fish are observed to adopt each other's kinematics for a short duration on a needs basis. This study explores the effect of such adaptive kinematics via a 2D computational model, focusing on the underlying fluid dynamics and propulsive performance. The effect of the shape is also studied by considering various series of NACA00XX hydrofoil, based on the fineness ratio (length/thickness) of different anguilliform and carangiform fish reported in the literature. Adaptation of carangiform (anguilliform) mode of undulation kinematics by an anguilliform (carangiform)-shaped hydrofoil is found to result in an increase (decrease) in the thrust coefficient along with a decrease (increase) in the quasipropulsive efficiency. Flow characteristics, such as the pressure distribution around the hydrofoil, the strength of the vortices, and the jet behind the hydrofoil, are correlated with the propulsive performance of two naturally observed and six adaptive cases mimicking anguilliform and carangiform fish-inspired shape and swimming. Fineness ratio and undulation wavelength, as compared to the amplitude envelope, has more influence on the propulsive performance and vortex strength in the wake, except for the protovortex, which is more influenced by the amplitude envelope. Finally, a discussion is presented to connect the present 2D CFD results with some of the observed behavior of the anguilliform/carangiform fish in nature. This bioinspired and biomimetics study on naturally observed and adaptive fish-inspired swimming may assist with the need-based efficient design of underwater vehicles.

*atulsharma@iitb.ac.in

DOI: 10.1103/PhysRevFluids.7.094102

I. INTRODUCTION

Each body/caudal fin (BCF) fish has evolved a certain combination of shape and kinematics (undulation wavelength and amplitude envelope) of its body/tail, suited for its propulsion and survival. For the undulation wavelength, Nangia *et al.* [1] reported that most BCF fish swim within a narrow range of wavelength that maximizes their swimming speed and thrust generation. However, within the reported optimal wavelength range, each BCF fish uses a certain combination of undulation wavelength, amplitude envelope, and shape of their body/tail. The individual kinematics and shape provide different advantages and abilities to various fish. Under certain conditions, a fish is also found to adapt the kinematics of another fish for a short duration. For example, the needlefish—an anguilliform swimmer—adapts the undulation wavelength of carangiform fish [2]. Similarly, another anguilliform swimmer, the eel, alters its wavelength according to speed [3]. Further, the leopard shark has a carangiform shape while it undulates like an anguilliform fish, possessing less than one wavelength along its body at any time [4]. Thus, adaptive kinematics is observed in nature for both anguilliform and carangiform fish.

The effect of such adaptive kinematics of two types of fish, anguilliform fish and carangiform fish, on the fluid dynamics and propulsive performance is the focus of the present study. Further, the effect of hypothetical—along with real—adaptive kinematics and the role of various shapes (of both the types of fish) are explored in our numerical study. The resulting study, on the separate and combined role of shape and kinematics, will be helpful in providing a fundamental understanding of the associated fluid flow, and also for the efficient and needs-based engineering design of the autonomous underwater vehicle (AUVs). Such a fish-inspired real and hypothetical adaptive kinematic-based hydrodynamic study is presented unique in the published literature.

The shapes of the body of anguilliform and carangiform fish are different, parameterized by a nondimensional fineness ratio $\mathrm{FR} = L/D$, defined as the ratio of the streamwise length L to maximum diameter D of a fish [5]. Anguilliform fish, such as eels and lamprey, have an elongated slender body $L \gg D$ (large FR) while carangiform fish, such as cod and herring, have a fusiform-shaped body (smaller FR) [5]. The kinematics of the body undulation of anguilliform and carangiform fish is represented by an amplitude envelope, $a(x)$, and wavelength, λ, of a traveling wave that passes along the body length. Anguiliform fish undulate their whole body while undulation is mostly restricted to the posterior part for carangiform fish. This is modeled with the amplitude envelope $a(x)$ that increases exponentially along the body for anguilliform fish [6] while it increases quadratically for carangiform fish [7]. At any time instant, an anguilliform fish possesses less than one wavelength traveling backwards along the body, $\lambda/L < 1$, while a carangiform fish possesses approximately one wavelength, $\lambda/L \sim 1$ [8].

CFD investigations of fish-inspired swimming are usually carried out by two different methodologies: tethered propulsion simulations and self-propelled simulations, corresponding to constant and varying swimming velocity, respectively. After reaching a periodic state in a self-propelled simulation, the propulsive velocity reaches an almost constant velocity similar to that obtained in a tethered propulsion simulation. However, at the periodic state, the mean thrust coefficient C_{Tm} is zero for self-propelled simulations and nonzero for tethered simulations. In the present study, tethered simulations are chosen over self-propulsion simulations along with a 2D hydrofoil-based 2D fish-inspired body instead of 3D fish shapes. Justification of these limitations of the present fish-inspired swimming model are discussed below in Sec. II C. Thus, for the present 2D study, the nondimensional parameters that govern the performance of an undulating swimmer are of three types: a hydrodynamic parameter (Reynolds number, Re); kinematic parameters (nondimensional maximum amplitude at the tail $A_{\max}$, and frequency St of undulation, undulation wavelength λ^*); and geometrical parameter (body shape). The nondimensional hydrodynamic and kinematic parameters

are defined as

$$\mathrm{Re} \equiv \frac{\rho u_p c}{\mu}, \ \mathrm{St} \equiv \frac{2 f a_{\max}}{u_p}, \ A_{\max} \equiv \frac{a_{\max}}{c}, \ \lambda^* \equiv \frac{\lambda}{c}, \tag{1}$$

where ρ is the density and μ is the dynamic viscosity of the surrounding fluid. Furthermore, c is the chord length of a NACA hydrofoil, f is the frequency of undulation, and $a_{\max}$ is the maximum amplitude of undulation at the tail.

The scope of the present literature survey covers experimental and numerical studies on the hydrodynamics of anguilliform and carangiform real-fish or fish-inspired swimming and focused on the effect of body shape, undulation wavelength, and amplitude envelope. Table I shows experimental and numerical studies for eels and lamprey as anguilliform fish; and saithe (pollock), mackerel, and mullet as carangiform fish. For the respective types of real (not NACA-based model) fish, the table shows reported values of the undulation wavelengths in the ranges $\lambda^* = 0.6$–0.87 and $\lambda^* = 0.95$–1.11; and the chordwise varying amplitudes $A(X)$ are exponential and quadratic.

There are various experimental studies on real and robotic fish. In an experimental study on real anguilliform fish, Müller *et al.* [3] observed that they can modify their body wave according to need—for high maneuverability or maximum swimming efficiency. Further, they also observed a new type of vortex structure traveling along with the body wave that was called a protovortex. Tytell and Lauder [6] studied the undulation kinematics of an anguilliform fish; and observed an exponentially increasing amplitude envelope of undulation when moving from the snout to the tail of the fish. For experimental observations on real carangiform fish, Videler and Hess [7] observed that fish with a larger amplitude and curvature near the peduncle generate larger speeds during undulations. Müller *et al.* [9] found that the anterior body undulation contributes about one-third of the total thrust generated by a carangiform fish. From robotic experimental studies, Hultmark *et al.* [10] observed that the wake structure behind an undulating robotic lamprey is similar to that of eels. Using a similar robotic lamprey, Leftwich and Smits [11] studied the pressure distribution on its surface and concluded that most of the thrust is generated from the posterior part of the body.

For fish-inspired undulating 2D NACA hydrofoils, there are more numerical studies than studies based on real shapes. Dong and Lu [12] performed FEM based 2D numerical simulations to study the effect of St on the hydrodynamic forces and the vortex structure of a fish-inspired undulating NACA0012 hydrofoil. Sui *et al.* [13] found that an undulating 2D NACA0012 hydrofoil starts generating net thrust force for $\mathrm{St} > 0.764$ at $\mathrm{Re} = 400$. Shao *et al.* [14] performed 2D numerical simulation for a fish-inspired undulating NACA0012 hydrofoil in the wake of a D-section cylinder. For $\mathrm{Re} = 1500$ and $\mathrm{St} = 0.13$ and 1.3, they observed that the thrust and wake structure behind the hydrofoil depends on the distance between the two bodies. Thekkethil *et al.* [15] performed 2D numerical simulations, with a unified kinematic model that encompasses both undulation of the body or/and pitching of the tail of various BCF fish and presented the thrust generation mechanism. Khalid *et al.* [16] studied the effect of λ^* and St on the hydrodynamic performance of anguilliform and carangiform swimming modes at $\mathrm{Re} = 100$, 1000, and 5000. They observed that anguilliform kinematics is more efficient at low Re, whereas the wavelength of a swimmer's wavy motion influences the propulsive performance at higher Re.

There are only a very few 3D numerical studies on an undulating fish-inspired body. Kern and Koumoutsakos [17] optimized the motion of anguilliform swimming to maximize its speed and efficiency. They reported that the tail generates most of the thrust when motion is optimized for fast swimming. In contrast, both body and tail contribute to the thrust when motion is optimized for efficient swimming. Borazjani and Sotiropoulos [18,19] found that the critical Strouhal number (St_c) at which the net force acting on the fish body becomes zero in a self-propelled simulation depends on Re, and the St_c decreases with increase in Re for both carangiform and anguilliform fish. With similar body shapes and undulation kinematics, Borazjani and Sotiropoulos [20] investigated the effect of adapting each other's kinematics for both anguilliform (lamprey) and carangiform (mackerel) fish. They found that the mackerel body is efficient in the viscous ($\mathrm{Re} \sim 10^2$) and inertial ($\mathrm{Re} \sim 10^3$) regime while the lamprey body is efficient in the transitional ($\mathrm{Re} \to \infty$) regime. Van

TABLE I. Summary of body shape, undulation wavelength λ^*, amplitude envelope $A(X)$, Reynolds number Re, and Strouhal number St used in the published literature and the present work for the hydrodynamics study on various types of anguilliform and carangiform fish.

Author	BCF fish and body shape	Undulation wavelength λ^*	Amplitude envelope $A(X)$	Re	St
Müller *et al.* [3]	Anguilliform, eel	0.69–0.87	—	≈10 000	≈0.56
Tytell and Lauder [6]		0.6		—	0.314–0.41
Hultmark *et al.* [10]	Anguilliform, lamprey robot	≈0.65	Exponential	115 000	0.65
Leftwich and Smits [11]				165 000	0.53
Borazjani and Sotiropoulos [18]	Anguilliform, lamprey			300, 4000, ∞	0–1.2
Videler and Hess [7]	Carangiform, saithe (pollock), mackerel	1.0	Quadratic	—	—
Müller *et al.* [9]	Carangiform, mullet	1.11		≈25 000	≈0.5
Borazjani and Sotiropoulos [19]	Carangiform, mackerel	0.95	Quadratic	300, 4000, ∞	0–1.2
Dong and Lu [12]	Carangiform,	1.0		5000	0.1–0.4
Sui *et al.* [13]	NACA0012			400	0.191–0.955
Shao *et al.* [14]	Carangiform, NACA0012	1.0	Quadratic	1500	0.13, 1.3
Khalid *et al.* [16]	Anguilliform and carangiform, NACA0012	0.5–1.5	Quadratic	100, 1000, 5000	0.1–0.8
Present study	Anguilliform NACA0006 and 0008 Carangiform NACA0012, 0018, and 0024 0024	0.65, 1	Exponential and quadratic	5000	0.6

Rees *et al.* [21,22] optimized the shape of an anguilliform swimmer and showed that the optimized shape outperformed real larval zebrafish for both speed and efficiency.

From the above literature survey, Table I documents anguilliform and carangiform fish-inspired swimming studies reported previously together with some studies based on a NACA0012 hydrofoil compared to the NACA00XX hydrofoil-based studies reported here. Overall, there appears to be

TABLE II. Fineness ratio reported in the literature, and appropriate NACA series hydrofoil analog proposed for different types of fish.

Reference	Fish	Fish type	Fineness ratio (FR)	Proposed NACA hydrofoil
Bainbridge [24]	Dace	Carangiform	6.7	NACA0015
	Trout	Carangiform	6.3	NACA0016
	Goldfish	Carangiform	4.5	NACA0022
Videler [5]	Cod	Carangiform	7.5	NACA0013
	Mackerel	Carangiform	8.8	NACA0011
	Eel	Anguilliform	21	NACA0005
Blake [25]	Cod	Carangiform	4.5–5	NACA0022–NACA0020
	Herring	Carangiform	4–5	NACA0025–NACA0020
Lim and Lauder [26]	Pacific hagfish	Anguilliform	18.667	NACA0005
	Robot			
Hultmark *et al.* [10], Leftwich and Smits [11]	Lamprey robot	Anguilliform	11.75	NACA0009
Present study	Modeled fish	Anguilliform	6.67–12.5	NACA0006, NACA0008
		Carangiform	8.33–4.17	NACA0012–NACA0024

almost no published work on the intrinsic relationship between shape and kinematics use by fish in nature, except that of Borazjani and Sotiropoulos [20] on adaptation of both λ^* and $A(X)$ for two adaptive swimmers: anguilliform fish adopting carangiform kinematics, and carangiform fish adopting anguilliform kinematics. The scope of our study is to investigate a much more comprehensive range of adaptive swimming cases by the systematic interchange of λ^* and $A(X)$, together as well as separately, between anguilliform-like and carangiform-like body shapes. Thus, instead of the constant fineness ratio considered previously [20], the present work considers the relevant range of FR reported in the literature for the different types of anguilliform and carangiform fish. This is shown in Table II. Representing the two naturally observed swimmers as AAA for anguilliform and CCC for carangiform swimming, we have adopted a three-letter notation: ACC stands for an anguilliform swimmer with adaptation of both wavelength λ^* and amplitude $A(X)$ of a carangiform swimmer. Further, separate adaptation of λ^* and $A(X)$ by anguilliform and carangiform-shaped swimmers, result in four more adaptive swimmers: ACA, AAC, CAC, and CCA. Here ACA and CAC (AAC and CCA) involve the adaptation of each other's undulation wavelength λ^* [amplitude $A(X)$] by the anguilliform and carangiform swimmers, respectively.

Thus, the objective of the present study is to explore the separate and combined roles of body shape FR, undulation wavelength λ^*, and amplitude envelope $A(X)$ on hydrodynamic performance for various types of anguilliform and carangiform fishlike body shapes and real as well as adaptive kinematics of a 2D hydrofoil. The fish are modeled here by different NACA hydrofoils, considering the fineness ratio as an overall representation of the general shape of a fish. The numerical study is done at reported undulation parameters of fish (Table I), i.e., at a constant frequency $\mathrm{St} = 0.6$, and maximum amplitude of undulations $A_{\max} = 0.1$ at a Reynolds number $\mathrm{Re} = 5000$. The present study is motivated by the hydrodynamic reasons behind three significant observations in nature: (i) why a particular combination of body shape, amplitude variation, and wavelength of undulation is used by different types of BCF fish, (ii) why anguilliform and carangiform fish alter their wavelength

for short periods on a needs basis, and (iii) why carangiform fish as compared to anguilliform fish have extra fins.

II. PROBLEM SETUP

A. NACA hydrofoil-based body-shape model for the BCF fish

The body shapes of the various types of anguilliform and carangiform fish are modeled here by NACA hydrofoils. This series was proposed by U.S. National Advisory Committee for Aeronautics (NACA); they are represented by NACA00XX, where XX refers to the percentage of the maximum thickness to the chord length of the hydrofoil. The present NACA hydrofoil-based body-shape model for BCF fish is justified since the distribution of volume is similar in both fish and foils [23].

As indicated above, the last two digits "XX" of a NACA00XX hydrofoil as a percentage give the inverse of the fineness ratio FR $= 1/(XX/100)$, defined above for the fish. For example, for a NACA0020 hydrofoil (with maximum thickness as 20% of the chord), FR $= 5$. The present body shape model-based NACA hydrofoils are based on the FR reported in the literature for anguilliform and carangiform fish: refer to Table II. The table shows that NACA005–NACA0009 correspond to the overall shape of anguilliform fish, while NACA0011–NACA0024 hydrofoils correspond to carangiform fish.

B. Kinematic models for BCF fish and quantities of interest

For the present 2D numerical simulations, the fish-inspired undulating hydrofoil is assumed to be neutrally buoyant and swimming unidirectionally with a constant velocity, u_p. For BCF fish, the lateral undulation of the body is modeled by a traveling-wave-based equation with increasing amplitude down the body [7], given as

$$\Delta y = a(x)\sin\left(\frac{2\pi x}{\lambda} - 2\pi f t\right), \tag{2}$$

where x is the streamwise coordinate from the leading edge of the hydrofoil, Δy is the lateral displacement of the hydrofoil, $a(x)$ is the amplitude envelope of undulation, which varies in the streamwise direction, λ is the wavelength of the traveling wave along the body, and f is the frequency of undulation. By using u_p as the velocity scale, and the chord length, c, as the length scale, the nondimensional form of Eq. (2) and associated body velocity V_{body} given [15] as

$$\Delta Y = A(X)\sin\left[2\pi\left(\frac{X}{\lambda^*} - \frac{\text{St}\,\tau}{2A_{\max}}\right)\right], \tag{3}$$

$$V_{\text{body}} = \frac{\pi\,\text{St}}{A_{\max}}A(X)\cos\left[2\pi\left(\frac{X}{\lambda^*} - \frac{\text{St}\,\tau}{2A_{\max}}\right)\right], \tag{4}$$

where $X = x/c$ and $Y = y/c$ are the nondimensional coordinates; $A(x) = a(x)/c$ is nondimensional amplitude envelope; and $\tau = tu_p/c$ is the nondimensional time. In addition, St, $A_{\max}$, λ^* (defined in Eq. (1)] are the nondimensional form of frequency, maximum amplitude and wavelength of undulation, respectively.

All types of BCF fish propel by generating a backward traveling wave [Eq. (3)]. However, the pattern of the traveling wave varies among the various types of BCF fish. Mathematically, these patterns are represented by Eq. (3) and are governed by the nondimensional wavelength λ^*, maximum amplitude of undulation $A_{\max}$, and amplitude envelope $A(x)$. The amplitude envelope variation over the body is exponential for an anguilliform fish and quadratic for carangiform fish, as discussed in the above literature review, given as

$$\text{Anguilliform:}\quad A(X) = 0.1\exp[\alpha(X-1)], \tag{5}$$

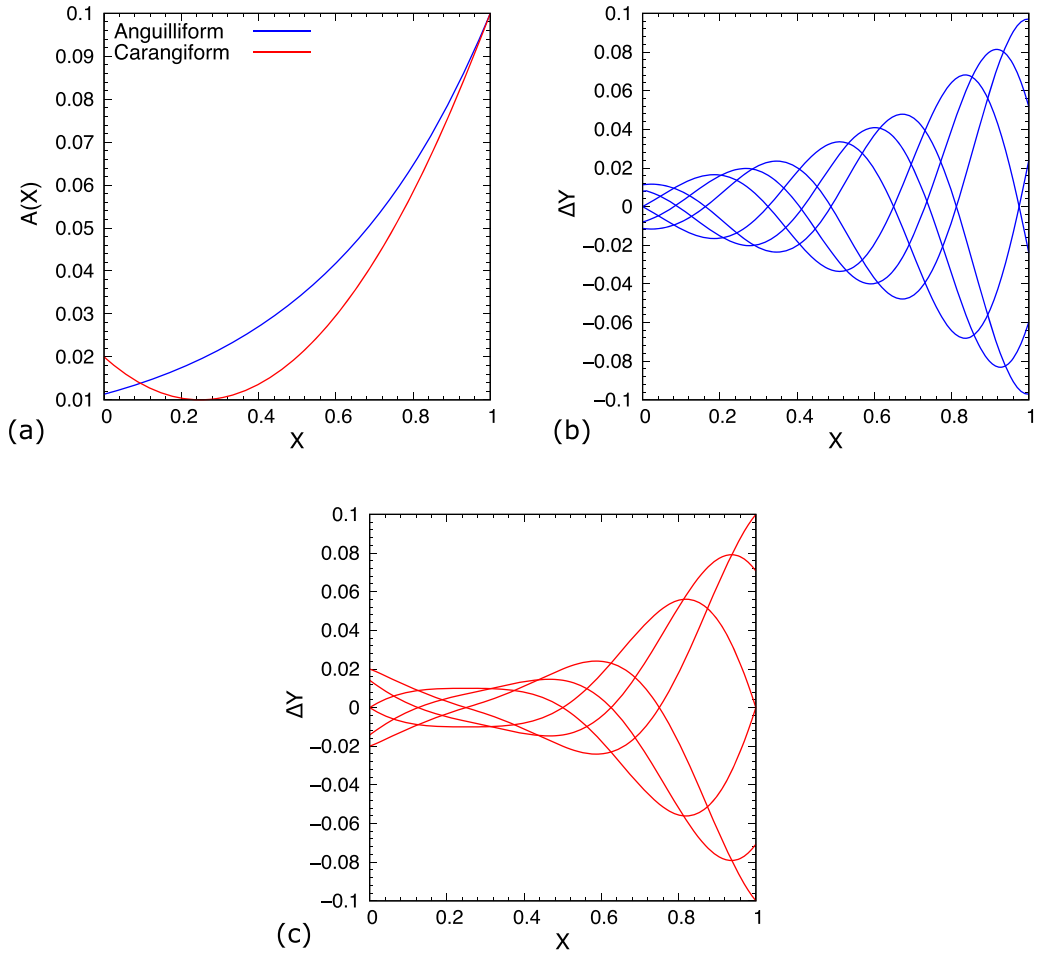

FIG. 1. Variation of (a) amplitude $A(X)$ [Eq. (5) and Eq. (6)] and (b, c) lateral displacement ΔY along the length of the fish (from head to tail). The ΔY is shown for the midline of the (b) anguilliform and (c) carangiform fish-inspired swimming using Eq. (3) at several time instances during one cycle of undulation.

$$\text{Carangiform:} \quad A(X) = a_0 + a_1 X + a_2 X^2, \tag{6}$$

where the amplitude growth rate (from head to tail of the body) is $\alpha = 2.18$, $A_{\max} = 0.1$ [Eq. (5)] and $\lambda^* \approx 0.65$ [Eq. (3)] for an undulating anguilliform fish [10]. On the other hand, for a carangiform fish, $a_0 = 0.02$, $a_1 = -0.08$, $a_2 = 0.16$ in Eq. (6) and $\lambda^* = 1$ in Eq. (3) [7,19]. The corresponding variation of the amplitude envelope $A(X)$ over the body for both types of fish is shown in Fig. 1(a). The figure shows that the maximum amplitude $A_{\max}$ occurs at the tail tip $X = 1$; substituting $X = 1$ in Eq. (5) and Eq. (6) results in $A_{\max} = 0.1$ for both fish. The amplitude of undulation is minimum at the head and increases while moving from head to tail for an anguilliform fish [Fig. 1(a)]. However, the amplitude is minimum at $0.23c$ from the head for a carangiform fish [Fig. 1(a)]. Moreover, it can be seen that the head movement is larger for the carangiform fish than for the anguilliform fish.

Figures 1(b) and 1(c) show the lateral displacement ΔY of the midline of the anguilliform and carangiform fish calculated at several time instants for one undulation cycle using [Eq. (3)], with the amplitude envelope $A(X)$ calculated by Eq. (5) for anguilliform and Eq. (6) for carangiform fish-inspired undulations. The figure shows undulation of the whole body for the anguilliform and mostly

posterior parts of the body for the carangiform fish. Since $\lambda^* = 0.65$ for lamprey/anguilliform and $\lambda^* = 1$ for mackerel/carangiform fish, the figure shows more than one wave traveling over the length of anguilliform fish as compared to one wave for a carangiform fish.

For the present tethered simulations-based results that correspond to a certain instantaneous transient self-propelled simulation (discussed in Sec. II C), the accelerating performance of the hydrofoil is presented here as the net streamwise and sidewise or lateral hydrodynamic forces acting on the hydrofoil (the respective forces per unit depth as thrust force F_T and lateral force F_L) and a quasipropulsive efficiency η_{QP}. In nondimensional form, the performance parameters are given as

$$C_T = \frac{F_T}{1/2\rho u_p^2 c}, \quad C_L = \frac{F_L}{1/2\rho u_p^2 c}, \tag{7}$$

$$\eta_{QP} = \frac{P_{\text{out}}}{P_{\text{in}}} = \frac{(F_{Ds} + F_{Tm})\, u_p}{\int f_l v_{\text{body}}\, ds} = \frac{C_{Ds} + C_{Tm}}{\int c_L V_{\text{body}}\, dS}, \tag{8}$$

where C_T is the thrust coefficient and C_L is the lateral force coefficient; the subscript m in C_{Tm} and F_{Tm} correspond to the time-averaged value. Further, ρ is the density of the surrounding fluid, u_p is the constant propulsive velocity, f_l is the local lateral force per unit surface area of the hydrofoil, and V_{body} is the lateral velocity of an undulating hydrofoil [Eq. (4)]. Also, F_{Ds} and C_{Ds} are the drag force and drag coefficient for a stationary straight NACA00XX hydrofoil in a free-stream flow at the same Re; and the product of F_{Ds} with u_p represents the power required to tow the stationary hydrofoil. Note that the propulsive velocity u_p in the present tethered simulation is equal to the free-stream velocity u_∞.

Also note that the above definition of η_{QP} was originally proposed by Maertens *et al.* [27] for the periodic state of both tethered and self-propelled simulations, and was later proposed for the transient state of the self-propelled simulations in a recent work from our research group [28]. Quasipropulsive efficiency η_{QP} is widely used by various researchers [28–31] and has an ability to predict similar results from tethered and self-propulsion simulations; this was demonstrated by Maertens *et al.* [27] for $\text{St} \geqslant 0.4$ and $\text{Re} = 5000$. Furthermore, being an inverse of the normalized cost of transport (CoT), η_{QP} also considers the effect of change of mass with body shape.

C. Computational model

The present computational model considers the 2D hydrofoil for the body of various anguilliform and carangiform fish, tethered simulations, and lateral as well as rotatory constraints for the fish-inspired body. The 2D hydrofoil model represents the body of a fish and does not consider the pectoral, dorsal, anal, pelvic, and caudal fin. In the literature, it is well established that simplified 2D models can help understand complex fish swimming behavior [15,16,28,32–34]. Further, some studies in the literature show that the results from the 2D simulations are comparable to the 3D results at the same set of governing parameters. In this context, Liu *et al.* [35] performed 3D simulations for flow over a tadpole and observed that the horizontal symmetrical midplane's pressure contours and velocity profiles are similar to their earlier 2D study [36]. Further, they also observed that the flow and pressure distribution over the tail is 2D, except for a small region limited to the dorsal and ventral tail fin. Gazzola *et al.* [37] performed both 2D and 3D simulations and observed similar trends for the circulation and area of the vortices shed by fish. Also, the efficiency and distance traveled by them were comparable. Further, they also noted that the optimized results from the 2D simulations match closely to the starting bout observed experimentally in larval fish zebrafish by Muller *et al.* [38]. Zurman-Nasution *et al.* [39] showed that the flow structure and forces are effectively 2D for a pitching NACA0016 hydrofoil (similar to an undulating hydrofoil with $\lambda^* \to \infty$ [15,28,33]) for St in the range 0.3–0.6 at $\text{Re} = 5300$. Thus, the above literature supports the 2D assumption of the present study for flow over undulating hydrofoils at $\text{St} = 0.6$ and $\text{Re} = 5000$.

In our recent self-propelled simulations-based study [33], we showed an asymptotic increase in the propulsive velocity u_p (that is due to an asymptotic decrease in the mean thrust coefficient C_{Tm} in

the transient state), where the asymptotic $C_{Tm}^{\text{net}} = 0$ (in the dynamic-steady or periodic state) leads to a constant u_p. However, a tethered simulation corresponds to a nonzero C_{Tm}^{net}-based increasing u_p or accelerating propulsion. The main disadvantage of self-propelled simulations is that the propulsive velocity u_p is an output performance parameter. This means that the Reynolds number and Strouhal number are different when comparing the propulsive performance of two hydrofoils with different shapes and kinematics, as in the present work. Alternatively, tethered propulsion simulations allow us to compare different shapes and kinematics of the hydrofoils at the same Re and St and are chosen here over self-propulsion, where our tethered simulation-based dynamic steady-state results can be considered to correspond to certain instantaneous self-propelled simulation-based transient results. This consideration seems reasonable since the self-propelled adaptive kinematics is observed in nature for a short duration, where the fish is likely to remain in a transient state. Recently, using the above assumptions for a similar problem on undulating hydrofoils performing different kinematics, a tethered simulation-based results was also reported recently by Khalid *et al.* [16].

D. Governing equations and computational details

A level set function-based immersed interface method (LS-IIM), proposed by Thekkethil and Sharma [40], is used here for the present 2D numerical simulations of various types of anguilliform and carangiform fish-inspired swimming. The temporal variation of the fluid-solid interface is obtained here by using a level-set function ϕ, defined as a signed normal function from the fluid-solid interface, and is calculated by using a minimum distance and winding algorithm. The negative values of ϕ represent solid cells whereas the positive values represent the fluid cells. The fluid dynamics is governed by the incompressible Navier-Stokes equation, given as

$$\text{Continuity:} \quad \boldsymbol{\nabla} \cdot \overrightarrow{\mathbf{U}} = 0, \tag{9}$$

$$\text{Momentum:} \quad \frac{\partial \overrightarrow{\mathbf{U}}}{\partial \tau} + \boldsymbol{\nabla} \cdot (\overrightarrow{\mathbf{U}}\,\overrightarrow{\mathbf{U}}) = -\boldsymbol{\nabla} P + \frac{1}{\text{Re}} \nabla^2 \overrightarrow{\mathbf{U}}, \tag{10}$$

where $\overrightarrow{\mathbf{U}} (\equiv \overrightarrow{\mathbf{u}}/u_p)$ is the nondimensional velocity vector and $P (\equiv p/\rho u_p^2)$ is the nondimensional pressure.

Using the finite-volume method to discretize the Navier-Stokes equations, the LS-IIM in-house code is based on a fully implicit pressure projection method on a collocated grid that utilizes the QUICK scheme for the advection term and the central-difference scheme for the diffusion term. Further, the level-set function is updated at each time step by using predefined undulation kinematics, and the interface boundary conditions are implemented directly at the boundary nodes by using this function.

Considering different NACA00XX as the top/dorsal view based 2D profile for various types of BCF fish, Fig. 2 shows the nondimensional computational setup for the present problem. The boundary condition at the inlet corresponds to a constant velocity $U = 1$. A free slip boundary condition is used to limit the computational domain in the lateral direction. A convective boundary condition with a nondimensional convective velocity $U_c = 1$ is used at the outlet. A no-slip boundary condition is employed at hydrofoil's surface since the fish-inspired body has an imposed deformed shape and position in time and no flow-induced deformations are considered.

A comprehensive verification as well as a validation study of the present LS-IIM based in-house code can be found in Thekkethil and Sharma [40], for various one-way and two-way coupled 2D fluid-structure interaction (FSI) problems. Furthermore, the code used here was recently applied for a series of 2D/3D study on tethered/self-propulsion simulations for fish-inspired swimming of a hydrofoil [15,28,41]. For the present 2D FSI problem, a code-verification study of the LS-IIM is presented in Fig. 3(a). The figure shows excellent agreement between the present and published results for the temporal variation of the thrust coefficient C_T and lateral force coefficient C_L over one undulation cycle, for a NACA0012 hydrofoil-based carangiform fish at $\lambda^* = 1$, $\text{St} = 0.4$, and $\text{Re} = 5000$. Note that the computational setup for the validation study is the same as discussed and

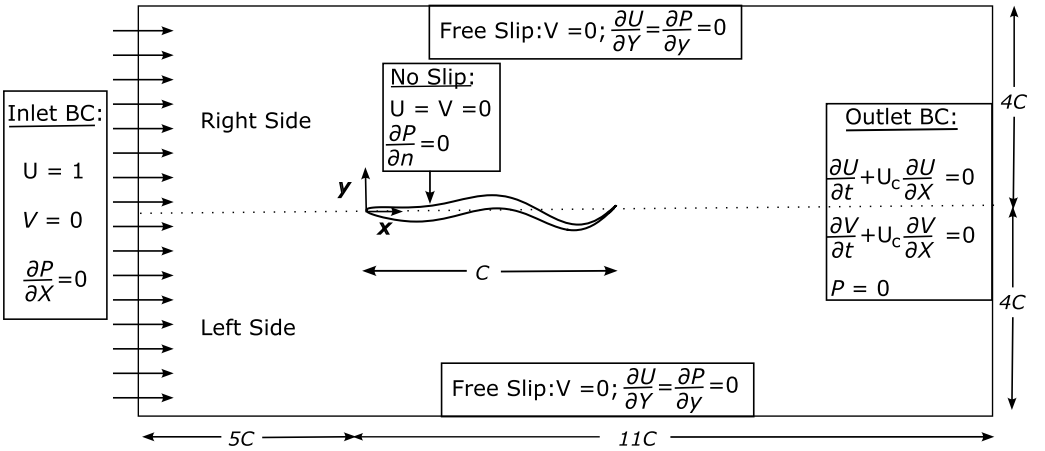

FIG. 2. Nondimensional computational setup for an undulating NACA00XX hydrofoil with constant propulsive velocity.

presented above in Fig. 2. Also, note that Fig. 3 shows the results after the flow reaches a periodic state, after the initial transient flow.

Further, for the carangiform fish-inspired undulation, a grid independence study is done by considering three Cartesian grid sizes: 382×142, 768×314, and 1543×588. For the respective grid sizes, the uniform finest grid cell sizes used were $\delta = 0.01$, 0.005, and 0.0025 near the undulating hydrofoil and the uniform coarse grid cell sizes were $\Delta = 0.5$, 0.25, and 0.125 far from the hydrofoil. A hyperbolic stretched nonuniform grid is used in the region that is between the uniform fine and coarse domains. For the two finer grid sizes as compared to the coarsest grid, Fig. 3(b) shows a much smaller difference in the temporal variation of the lift coefficient. Thus, the intermediate grid size of 718×314 is used here for all the simulations presented below. This has 400 cells across the chord of the hydrofoil.

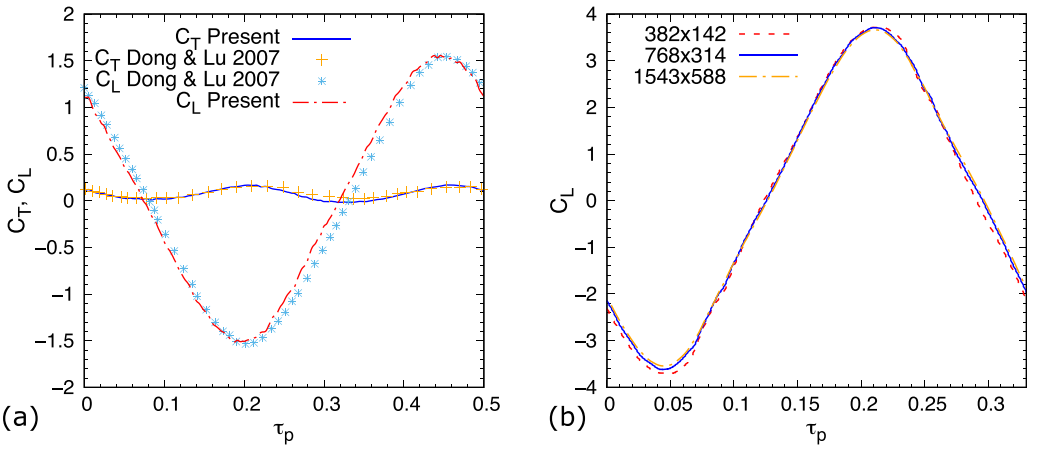

FIG. 3. (a) Code verification study and (b) grid independence study. Temporal variation of (a) thrust coefficient C_T and (a, b) lift coefficient C_L, after the flow reaches to a periodic state, at $\lambda^* = 1$ and $\mathrm{Re} = 5000$. For a carangiform fish-inspired undulating NACA0012 hydrofoil, the Strouhal number is 0.4 (a) and 0.6 (b). Here $\tau_p = 0$ corresponds to a time instant after the flow reaches a periodic state.

TABLE III. Various nondimensional governing input parameters considered in the study.

BCF fish	Governing parameters	
Anguilliform	Shape	NACA0006, NACA0008
	Undulation wavelength	$\lambda^* = 0.65$
	Amplitude envelope	$A(X) = 0.1\exp[2.18(X-1)]$
Carangiform	Shape	NACA0012, NACA0018, NACA0024
	Undulation wavelength	$\lambda^* = 1.00$
	Amplitude envelope	$A(X) = 0.02 - 0.08X + 0.16X^2$

E. Parametric details

After demonstrating code verification and grid independence of the present numerical methodology, the LS-IIM-based in-house code is employed for studying the present problem. Note that the hydrofoil is assumed to be neutrally buoyant. The assumptions are reasonable for almost all anguilliform fish, and also for carangiform fish, such as tuna.

For the present numerical investigation on the various types of anguilliform and carangiform fish-inspired swimming, various nondimensional governing input parameters are shown in Table III:

Note that these parameters are chosen to be similar to those used in previous works and correspond closely to real swimming conditions for the two types of BCF fish. Considering all possible combinations of λ^* and $A(X)$ for the anguilliform and carangiform fish-inspired bodies, Fig. 4 presents the eight different cases studied here.

III. EFFECT OF ADAPTATION OF ALTERNATIVE UNDULATION WAVELENGTH AND AMPLITUDE ENVELOPE ON PROPULSIVE PERFORMANCE

For a constant nondimensional maximum amplitude $A_{\max} = 0.1$ and frequency of undulation $\mathrm{St} = 0.6$ at a Reynolds number $\mathrm{Re} = 5000$, this section presents the effect of the adaptation of each other's undulation wavelength λ^* and/or amplitude envelope $A(X)$ on the propulsive performance of various types of anguilliform and carangiform fish-inspired swimming hydrofoils. Note that the time-averaged performance parameters after reaching a pure periodic state, were calculated over 20 cycles of the periodic flow.

A. Effect of the adaptation of undulation wavelength λ^*-based kinematics

The adaptation involves an increase (decrease) in λ^* from 0.65 (1) to 1 (0.65) for anguilliform (carangiform) fish-inspired swimming of a hydrofoil, which has a thinner (thicker) body and exponentially (quadratically) varying amplitude $A(X)$ of undulation: Figs. 4(a) and 4(b) and 4(e) and 4(f). The effect of the adaptation of λ^*-based kinematics is studied here for the propulsive performance of the resulting two adaptive cases (ACA and CAC) as compared to the two natural observed cases (AAA and CCC) of anguilliform and carangiform fish swimming that is modeled here with the hydrofoil-based 2D tethered simulations. The results are shown in Fig. 5, for the variation of η_{QP}, C_{Tm}, and C_{Lrms} with increasing (decreasing) λ^* of the thinner (thicker) hydrofoil for anguilliform (carangiform) fish-inspired swimming.

For various anguilliform fishlike-shaped hydrofoils (NACA0006 and NACA0008), the figure shows that the adaptation of λ^* leads to a reduction in η_{QP} while the magnitude of C_{Tm} and C_{Lrms} increases significantly; compare ACA with AAA in Fig. 5. However, η_{QP} is yet larger and C_{Lrms} is smaller for the adaptive ACA as compared to the carangiform fish-inspired undulating hydrofoil; compare ACA with CCC in the figure. Thus, there is an opportunity for anguilliform fish-inspired-shaped hydrofoils to generate more thrust by undulating with a larger λ^* [Figs. 5(a) and 5(b)]. The larger thrust, however, comes at the cost of smaller η_{QP} and larger C_{Lrms} for the

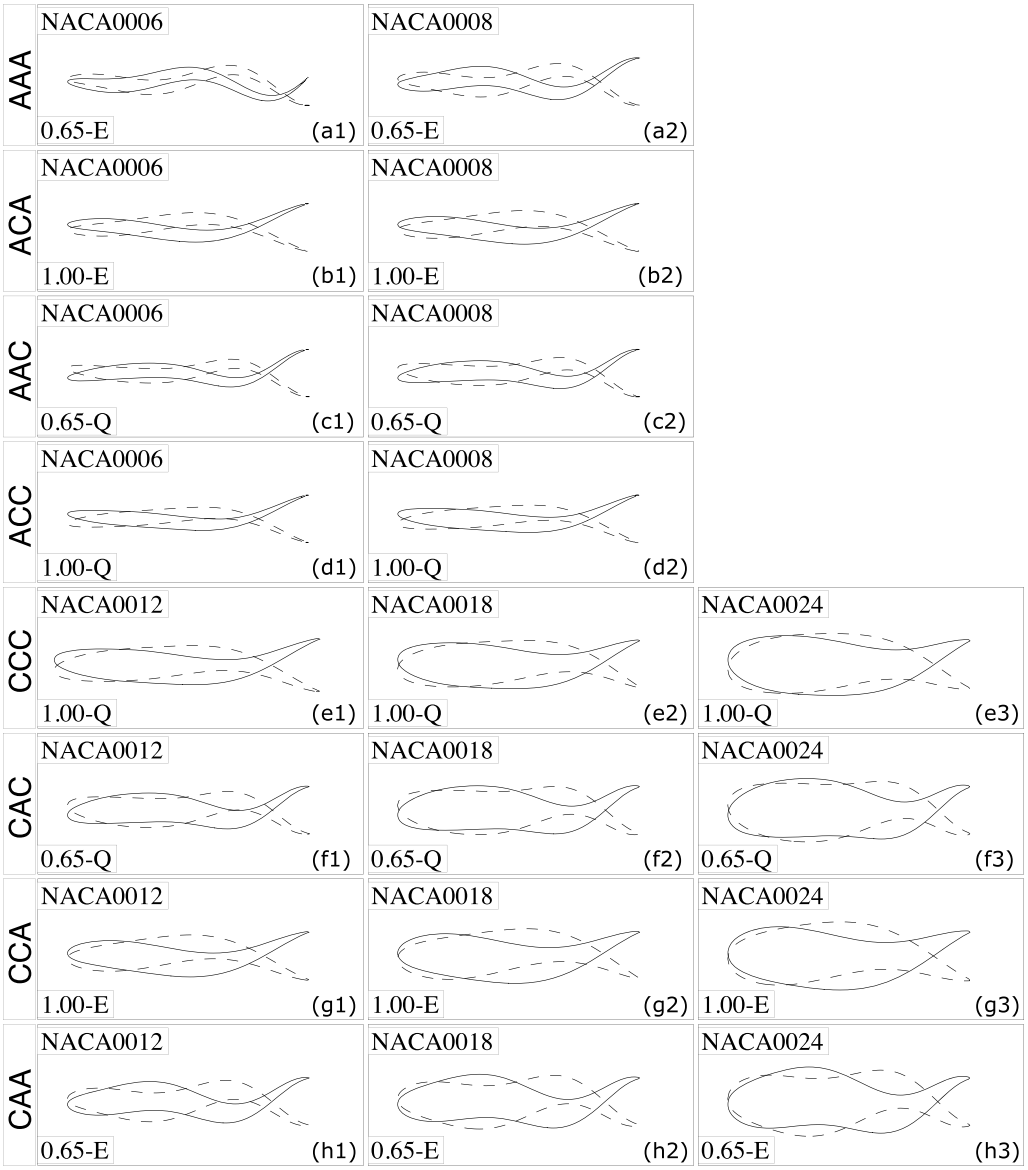

FIG. 4. Anguilliform (AAA) and carangiform (CCC) fish-inspired undulating hydrofoils, at the extreme left/right tail position, with an adaptation of each other's undulation wavelength λ^* (ACA and CAC), exponential/quadratic amplitude envelope $A(X)$ (AAC and CCA), and λ^* as well as $A(X)$ (ACC and CAA). In each panel NACA00XX corresponds to the shape, 0.65/1.00 represents λ^*, and E/Q corresponds to exponential/quadratic-based amplitude envelope.

ACA as compared to AAA [Fig. 5(c)]. The larger C_{Lrms} would requires an additional mechanism to stabilize the body in view of the larger amplitude of the temporal variation in the lateral force [Fig. 5(c)].

Figure 5 shows that the adaptation of smaller λ^*-based kinematics for various carangiform fishlike-shaped hydrofoils (NACA0012, NACA0018, and NACA0024) has an opposite effect to that discussed above for the anguilliform fish-inspired-shaped hydrofoil, with an increase in η_{QP}

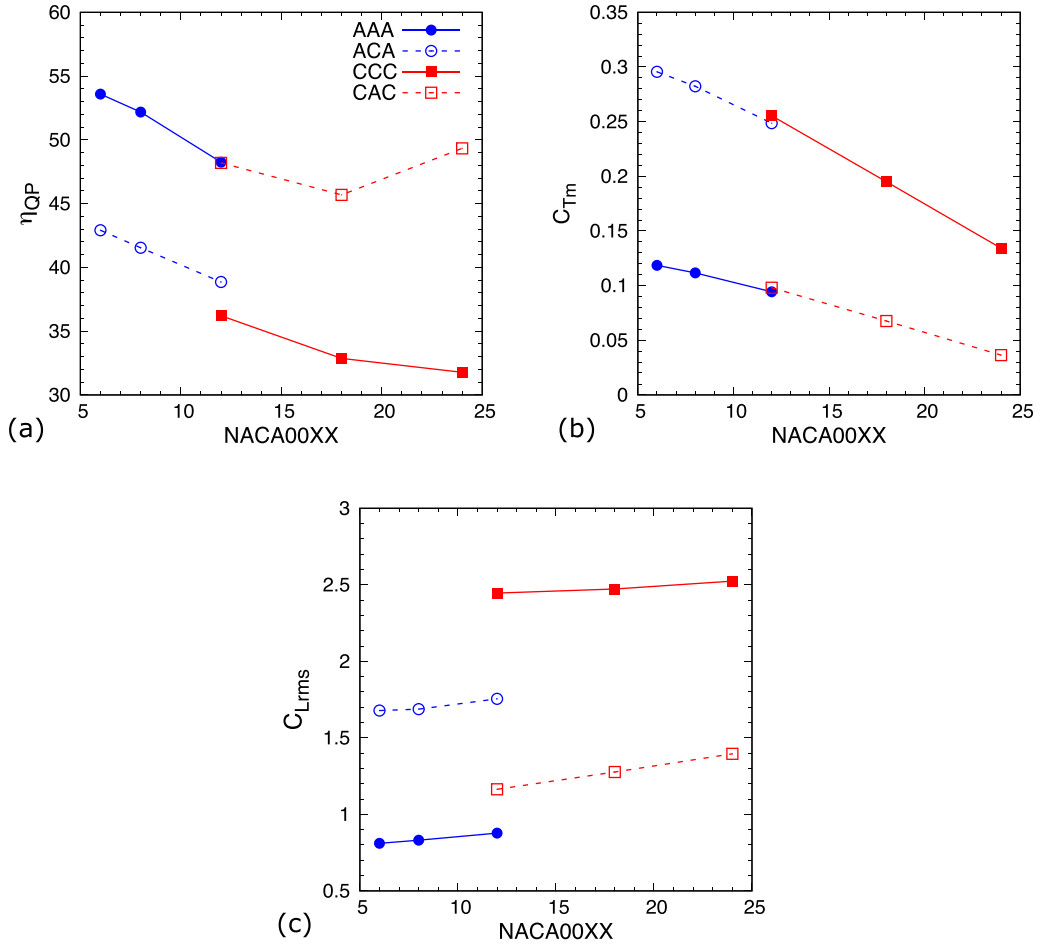

FIG. 5. Variation of (a) quasipropulsive efficiency η_{QP}, (b) mean thrust coefficient C_{Tm}, and (c) rms value of lateral force coefficient C_{Lrms} for various types of anguilliform and carangiform fish-inspired swimming foils, at Re = 5000, St = 0.6, and $A_{\max} = 0.1$. The adaptation leads to increase in λ^* from 0.65 to 1.00 for anguilliform and vice versa for carangiform fish.

and a decrease in C_{Tm} as well as C_{Lrms} for the adaptive CAC as compared to the natural observed CCC case. Further, the adaptation leads to almost the same or smaller η_{QP} and C_{Tm} while C_{Lrms} is larger for the adaptive CAC as compared to the anguilliform case; –compare CAC with AAA in the figure, indicating the role of $A(X)$, presented below. The present finding is supported by a subcarangiform fish, which possesses a body shape like a carangiform fish and undulates continuously with wavelength close to an anguilliform fish.

Thus, the adaptation of each other's λ^*-based kinematics is demonstrated here to be more thrust-generating for the anguilliform and more efficient for the carangiform fish-inspired hydrofoils. This is supported by published literature that reports such adaptation for anguilliform fish, as discussed further in Sec. V. Further, the present result of the increase in C_{Tm} with λ^* is consistent with that reported in the literature [1,15].

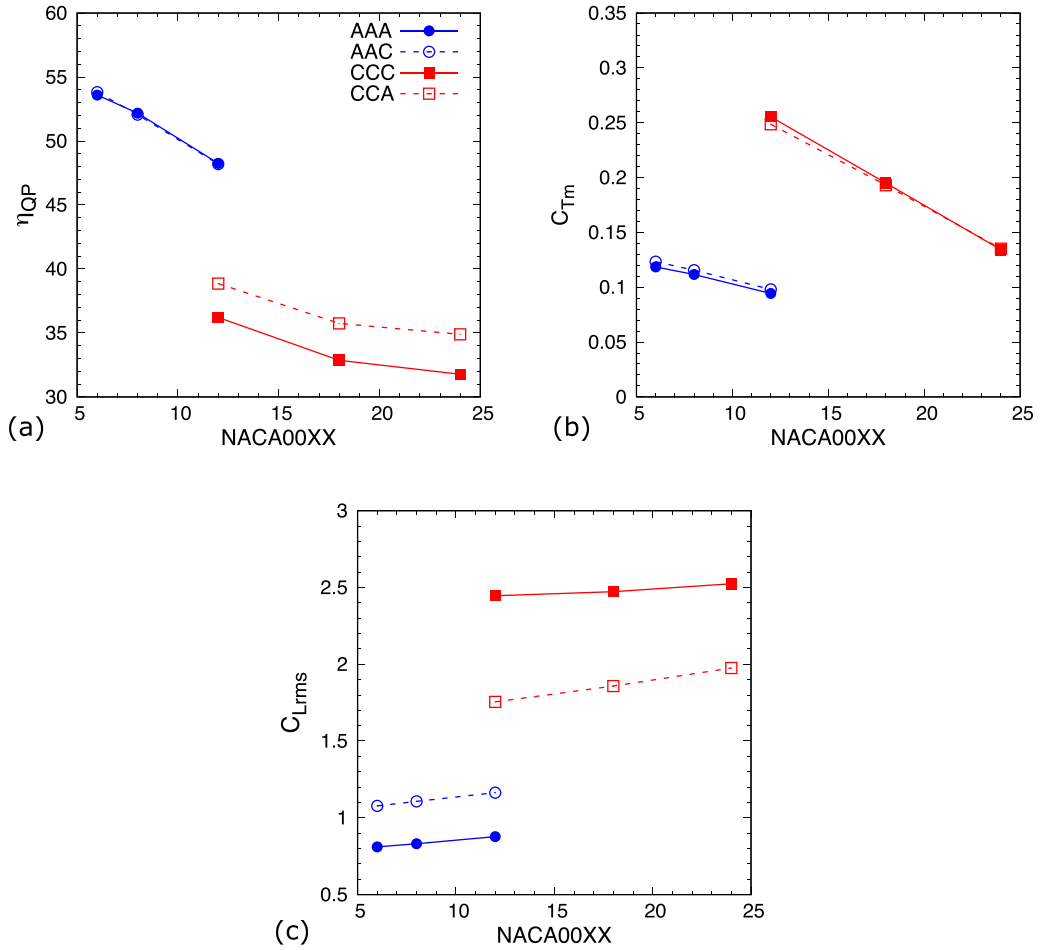

FIG. 6. Variation of (a) quasipropulsive efficiency η_{QP}, (b) mean thrust coefficient C_{Tm}, and (c) rms value of lateral force coefficient C_{Lrms} for various types of anguilliform and carangiform fish-inspired swimming foils, at Re $= 5000$, St $= 0.6$, and $A_{\max} = 0.1$. The adaptation leads to interchange of exponential to quadratic amplitude envelope $A(X)$ for anguilliform and vice versa for carangiform fish.

B. Effect of the adaptation of amplitude envelope $A(X)$-based kinematics

The adaptation involves the change in the equation for amplitude $A(X)$ from exponential (quadratic) to quadratic (exponential) for anguilliform (carangiform) fish-inspired propulsion of the hydrofoil, which has thinner (thicker) body shape and smaller (larger) λ^*: Figs. 4(a) and 4(c) and 4(e) and 4(g). The propulsive performance of the resulting adaptive cases (AAC and CCA) as compared to the naturally observed cases (AAA and CCC) is shown in Fig. 6 for the variation of η_{QP}, C_{Tm}, and C_{Lrms} of various NACA00XX hydrofoil-based anguilliform and carangiform fish-inspired swimming.

For various anguilliform fishlike-shaped foils (NACA0006 and NACA0008), Fig. 6 shows that the adaptation of $A(X)$ leads to almost the same η_{QP} and C_{Tm} while C_{Lrms} increases significantly; compare the results for AAC with AAA in this figure. This increase of lateral forces can make anguilliform swimming unstable since they do not have extra fins as a stability mechanism. The better lateral stability could be the reason for the exponential $A(X)$ by anguilliform fish in nature. For the various carangiform fishlike-shaped hydrofoils (NACA0012, NACA0018, and NACA0024),

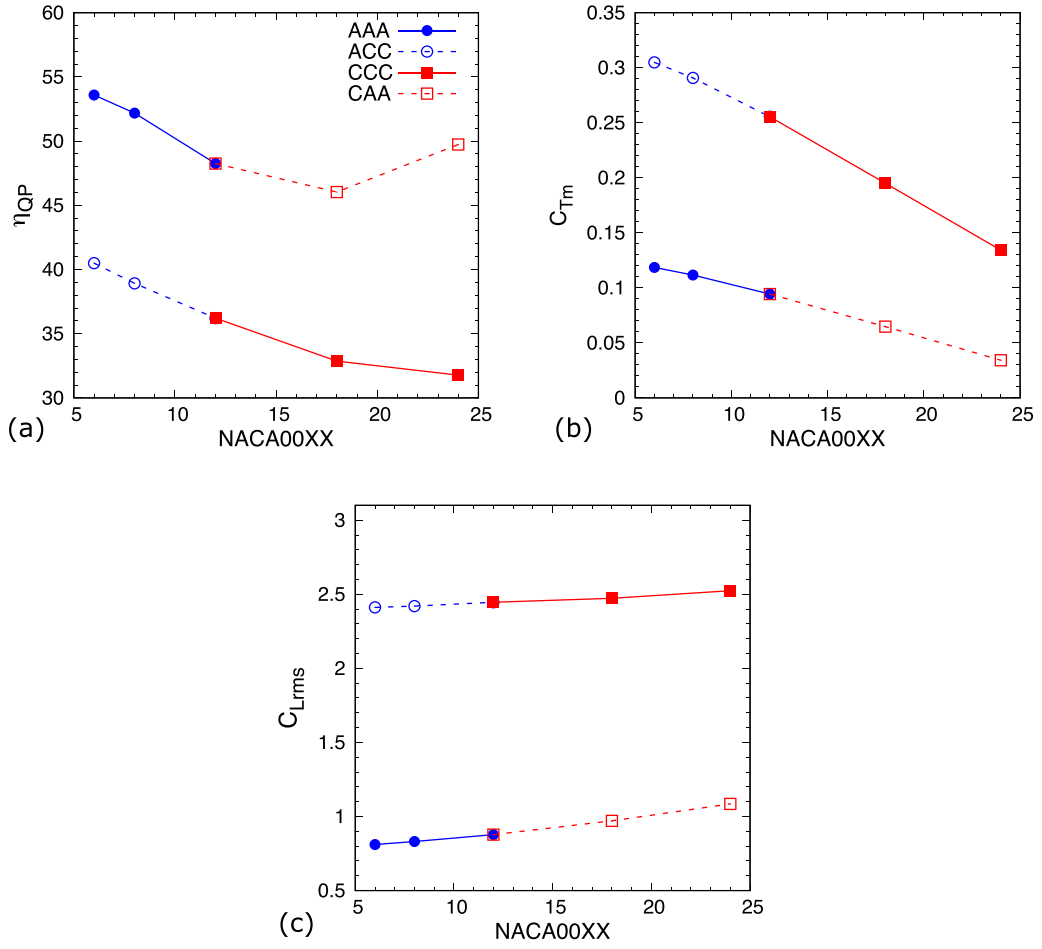

FIG. 7. Variation of (a) quasipropulsive efficiency η_{QP}, (b) mean thrust coefficient C_{Tm}, and (c) rms value of lateral force coefficient C_{Lrms} for various types of anguilliform and carangiform fish-inspired swimming foils, at Re $= 5000$, St $= 0.6$, and $A_{\max} = 0.1$.

the figure shows a slight increase in η_{QP} with almost same C_{Tm} and a decrease in the C_{Lrms} while undulating with the exponential $A(X)$ based anguilliform-like amplitude envelope; compare the results for CCA and CCC in this figure.

In summary, the adaptation of amplitude envelope $A(X)$ does not much affect on the mean thrust, but it alters the stability of the locomotion significantly—less stable for the anguilliform and more stable for the carangiform fish-inspired-shaped hydrofoils. However, for carangiform-shaped hydrofoils, the adaptation provides more efficient propulsion. Note that the results for the real AAA and the adaptive CAA (also for CCC and ACC) fish cases are continuous in Fig. 7, while that for the real AAA and adaptive CAA (also for CCC and ACC) fish cases are discontinuous in Fig. 6; for all the parameters. However, such variation for a real and adaptive fish case are continuous in Fig. 5(b) for C_{Tm} and discontinuous in Fig. 5(c) for C_{Lrms}.

C. Effect of the adaptation of both λ^* and $A(X)$-based kinematics

The adaptation for an anguilliform (carangiform) fish-inspired-shaped hydrofoil involves a larger (smaller) $\lambda^* = 1$ ($\lambda^* = 0.65$) and quadratic (exponential) variation in the streamwise-varying

amplitude $A(X)$ of undulation: Figs. 4(a) and 4(d) and 4(e) and 4(h). The effect of the adaptation of both λ^* and $A(X)$ is studied here for the propulsive performance of the resulting two adaptive cases (ACC and CAA) as compared to the two naturally observed cases (AAA and CCC). This is shown in Fig. 7 for the variation of η_{QP}, C_{Tm}, and C_{Lrms} with increasing thickness of a NACA00XX hydrofoil for various types of anguilliform and carangiform fish-inspired swimming.

For various anguilliform fishlike-shaped hydrofoils (NACA0006 and NACA0008), comparing ACC and AAA in Fig. 7 shows that the adaptation of λ^* and $A(X)$ reduces the η_{QP} while the magnitudes of C_{Tm} and C_{Lrms} increase significantly; similar to the result presented for ACA and AAA in Fig. 5. For the carangiform fishlike-shaped hydrofoils (NACA0012, NACA0018, and NACA0024), comparing CAA and CCC in the figure shows a reduction in the magnitudes of C_{Tm}, and C_{Lrms} while η_{QP} increases significantly; similar to the result presented for CAC and CCC in Fig. 5. Thus, the adaptation of λ^* and both λ^* and $A(X)$ does not leads to any hydrodynamic advantage other than providing better lateral stability to the swimming motion. The figure also shows that the AAA fish-inspired swimming is far more efficient and stable than the other cases here although AAA swimming generates less thrust.

Figures 5–7 also show the effect of foil thickness (FR) on the performance of a fishlike undulating hydrofoil. For all the undulation kinematics combinations, C_{Tm} and η_{QP} increase with a reduction in thickness of the hydrofoil, except for carangiform shapes with anguilliform's λ^* (CAC and CAA), where η_{QP} is slightly higher for the shape corresponding to NACA0024 as compared to NACA0018 hydrofoil. A similar trend was observed by Van Rees *et al.* [21] while performing 3D simulations for anguilliform kinematics. Further, for an oscillating hydrofoil at $\mathrm{Re} = 5000$ and $\mathrm{St} = 0.3$, Van Buren *et al.* [42] reported a similar variation for C_{Tm} while comparing NACA0010, NACA0012, and NACA0020 (approximately 1% reduction in C_{Tm} with an increase in 1% of thickness). However, the reported variation for efficiency (η_T) is different since they documented that the highest efficiency is for NACA0012. It is important to note that they used Froude efficiency compared to the quasipropulsive efficiency used in the present study.

Therefore, by comparing the results from Secs. III A, III B, and III C, one can conclude that the shape and undulation wavelength λ^* as compared to amplitude envelope $A(X)$ are found to dominate thrust generation C_{Tm}; whereas the amplitude envelope $A(X)$ has a significant effect on lateral stability.

IV. EFFECT OF THE ADAPTATIONS ON FLOW CHARACTERISTICS

The above discussed propulsive performance parameters describe an engineering effect that is caused by scientifically exciting flow characteristics. For a comprehensive cause-and-effect based CFD analysis [43], the hydrodynamic cause for the engineering effect of the adaptation of each other's undulation wavelength and/or amplitude envelope by anguilliform and carangiform fish-inspired locomotion is presented in this section with the help of flow characteristics as contours of instantaneous pressure, instantaneous vorticity, and time-averaged streamwise velocity.

Along with the 2D flow patterns, the flow characteristics are presented as 1D line plots for streamwise variation of the strength as well as position of both shed vortices and the streamwise jet behind the hydrofoil. Here the strengths of the shed vortices and the jet correspond to the local maximum of the instantaneous vorticity (found at the center of the vortex) and maximum time-averaged streamwise velocity $\langle U \rangle_{\max}$ at a streamwise location x, respectively. Further, the position corresponds to the x-y coordinate of the center of the shed vortex and x-y of the $\langle U \rangle_{\max}$ for the jet; here, the origin of the x-y coordinate system is shown in Fig. 2. Also notice the left and right sides of the foil in the figure.

A. Pressure characteristics near the hydrofoil

Whenever a fish initiates undulations, two types of hydrodynamic forces oppose its motion—a pressure force that acts normal to its surface and a viscous drag that acts tangentially to the

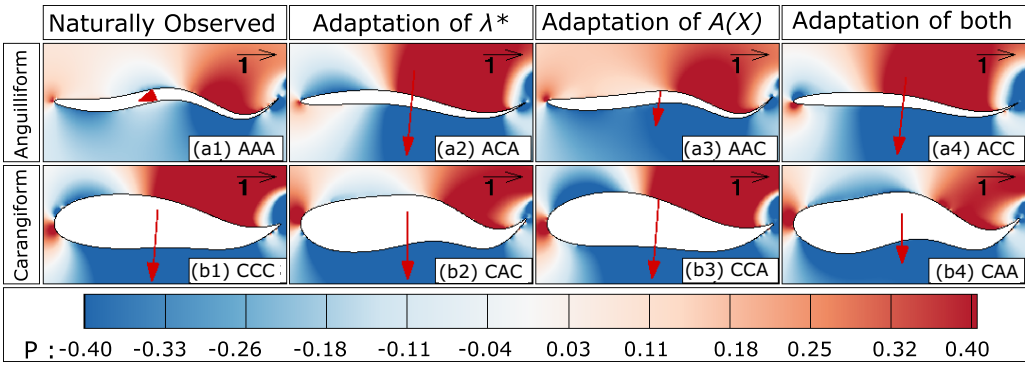

FIG. 8. Variation in the instantaneous pressure contours with the adaptation of each other's (a2, b2) λ^*, (a3, b3) $A(X)$, and (a4, b4) both λ^* and $A(X)$ by anguilliform and carangiform fish-inspired swimming foils, at $\mathrm{Re} = 5000$, $\mathrm{St} = 0.6$, and $A_{\max} = 0.1$. The red arrow represents the resultant force coefficient C_R along with its scale shown.

surface over the whole body. Thus, the undulation has to alter the surrounding flow such that the hydrodynamic forces act towards the propulsion direction for its locomotion. A BCF fish produces these forces by swimming such that it generates a backward-traveling wave along its body. Based on the wavelength λ^* of this backward-traveling wave, a number of time-varying crest-and-trough regions develop that travel along the body. While traveling, the crest pushes and the trough sucks the surrounding fluid. These suction and pushing actions accelerate the surrounding fluid and thus, develop positive or negative pressure zones across the flexure regions of the body, as seen for the present fish-inspired 2D model in Fig. 8. The figure shows that the resulting pressure gradient exerts a resultant hydrodynamic force C_R on the body whose component in the streamwise direction provides the required thrust force for propulsion. Since the required pressure thrust force is generated by periodically sucking and pushing of the surrounding fluid, this mechanism of thrust generation is known as the pressure suction mechanism [44].

The variation in the pressure and velocity near the hydrofoil in Fig. 8, for the naturally observed as compared to adaptive case is due to the difference in undulation kinematics that occurs with a change in the undulation wavelength λ^*, amplitude envelope $A(X)$, and both λ^* and $A(X)$ of the hydrofoil. The pressure contours shows a positive stagnant pressure zone near the head of the hydrofoil, whereas both negative and positive pressure zones are distributed along the crest-and-trough regions of the hydrofoil. The positive pressure zones are developed on those flexure regions where the fluid is pushed while the negative zones are developed where the surrounding fluid is sucked.

The magnitude of the pressure force generated across the flexures of the hydrofoil depends upon the volume of fluid being sucked and pushed. For undulations, this volume of fluid depends upon the surface area of crest-and-trough regions: the larger the surface area, the more the fluid is accelerated, and the larger will be the pressure difference across the front and rear of the hydrofoil, and, thus, the larger will be the thrust generation. One can observe a similar situation by comparing the naturally observed cases of AAA and CCC in Figs. 8(a1) and 8(b1). The figure shows that the magnitude of the streamwise pressure difference across the hydrofoil is larger for CCC than AAA. The larger pressure difference is due to the larger instantaneous lateral surface area offered by carangiform as compared to anguilliform fish-inspired NACA hydrofoils.

It is interesting to observe that even with the same shape, the projected lateral surface area is different for hydrofoils with different λ^* as their instantaneous shapes are different. Figure 8 shows that the instantaneous shape of the hydrofoil is of an S-type for cases with the smaller λ^* (AAA, CAC, and CAA), while the shape is of a C-type for cases with the larger λ^* (CCC, ACA, and

ACC). Here the S-type shape refers to an instantaneous shape with both crest and trough, while either crest or trough is present at any time instant for the C-type shape. Thus, a larger surface area is available for fluid-structure interaction in any lateral direction for C-type as compared to the S-type shape [35]. A larger surface area interacts with a larger volume of surrounding fluid; thus, the net force generation (C_{Tm}, C_{Lrms}) from the hydrofoil is larger for CCC and ACA that undulate with larger λ^* (Fig. 5). The present results with C-type and S-type instantaneous shapes of the undulating hydrofoil are consistent with those published by Liu *et al.* [35]. The increase in interaction with the surrounding fluid not only increases the magnitude of pressure thrust force generation, but also increases the input power required for undulations, since the hydrofoil has to displace a larger amount of fluid. Thus, depending upon the relative increase of C_{Tm} and P_{in}, the quasipropulsive efficiency either increases or decreases with λ^* of the hydrofoil. Note that the same mechanism was presented as a velocity mechanism by Bale *et al.* [45], for an undulating 3D body in a stationary fluid, where a larger wave speed V_w ($V_w = \lambda^* \times f$) of undulation leads to a larger momentum transfer to the surrounding fluid and an increase in the thrust coefficient C_T. For anguilliform-shaped hydrofoils, the adaptation of λ^*-based increase in input power is much higher than increase in thrust-production-based output power from the hydrofoil that results in reduction in the quasipropulsive efficiency for ACA as compared to AAA [Fig. 5(a)]. However, for carangiform shapes, the adaptation of λ^*-based loss in thrust generation is much smaller than the reduction in the input power required for propulsion that results in the enhancement of quasipropulsive efficiency for CAC as compared to CCC [Fig. 5(a)].

For the adaptive cases as compared to the real cases, Fig. 8 shows that the hydrofoil's overall instantaneous shape (S-type or C-type) interchanges with the adaptive-λ^* cases (ACA, ACC, CAC, and CAA) while it remains almost unchanged for the adaptation of $A(X)$ only cases (AAC, CCA). Thus, there is no significant effect of adopting each other's $A(X)$ on C_{Tm} [Fig. 6(b)]. While for the other cases, C_{Tm} increases for the adaptive anguilliform (ACA and ACC) and decreases for the adaptive carangiform cases (CAC, CAA); refer to Figs. 5(b) and 7(b). However, for the adaptive-λ^* cases (ACA, ACC, CAC, and CAA), the lateral deviation of the anterior and posterior parts of the hydrofoil increases and decreases for the adaptive anguilliform and carangiform fish-inspired hydrofoil, respectively. Thus, for the respective adaptive case, there is an increase and decrease in the instantaneous lateral coefficient C_L and C_{Lrms}; refer to Figs. 5(c), 6(c), and 7(c).

B. Vorticity and streamwise velocity characteristics

A signature of the thrust generation is seen in the flow pattern behind the hydrofoil, with a reverse von Kármán vortex street and jet formation. The respective flow patterns are shown in Fig. 9 and Fig. 10 for the naturally observed and adaptive anguilliform and carangiform fish-inspired swimming. The time instant for the instantaneous vorticity contours corresponds to the mean position of the hydrofoil, with the onset of tail tip motion in the left direction.

A result similar to that for the present single row of reverse von Kármán street has also been reported in the experimental studies for real anguilliform fish, like eels [46], lampreys [47], and for real carangiform fish, like rainbow trout [44], mullet [9,48], giant danio [49], and mackerel [50]. However, Müller *et al.* [3] has observed a double row reverse von Kármán vortex street in the wake of an undulating eel. The reason for this discrepancy has been explained by Videler *et al.* [48], as eels use a different undulation pattern for different swimming conditions. These results from the literature also shows that the swimming pattern changes the vortex structure behind an undulating body. For naturally observed carangiform (CCC), as compared to naturally observed anguilliform (AAA) fish-inspired swimming, a greater strength of the CW shed vortices and a larger velocity of the jet can be observed in Fig. 9(q) and Fig. 10(q), respectively.

Figure 9 [(a) and (b); (i) and (j)] shows another difference with the flow pattern behind the hydrofoil as symmetric for AAA [Figs. 9(a) and 9(b)] and asymmetric for CCC [(Figs. 9(i) and 9(j)] fish-inspired swimming; this can be judged quantitatively by comparing their position of the center of CW vortices in Fig. 9(r). A similar asymmetric wake was also observed by Khalid *et al.* [16]. The

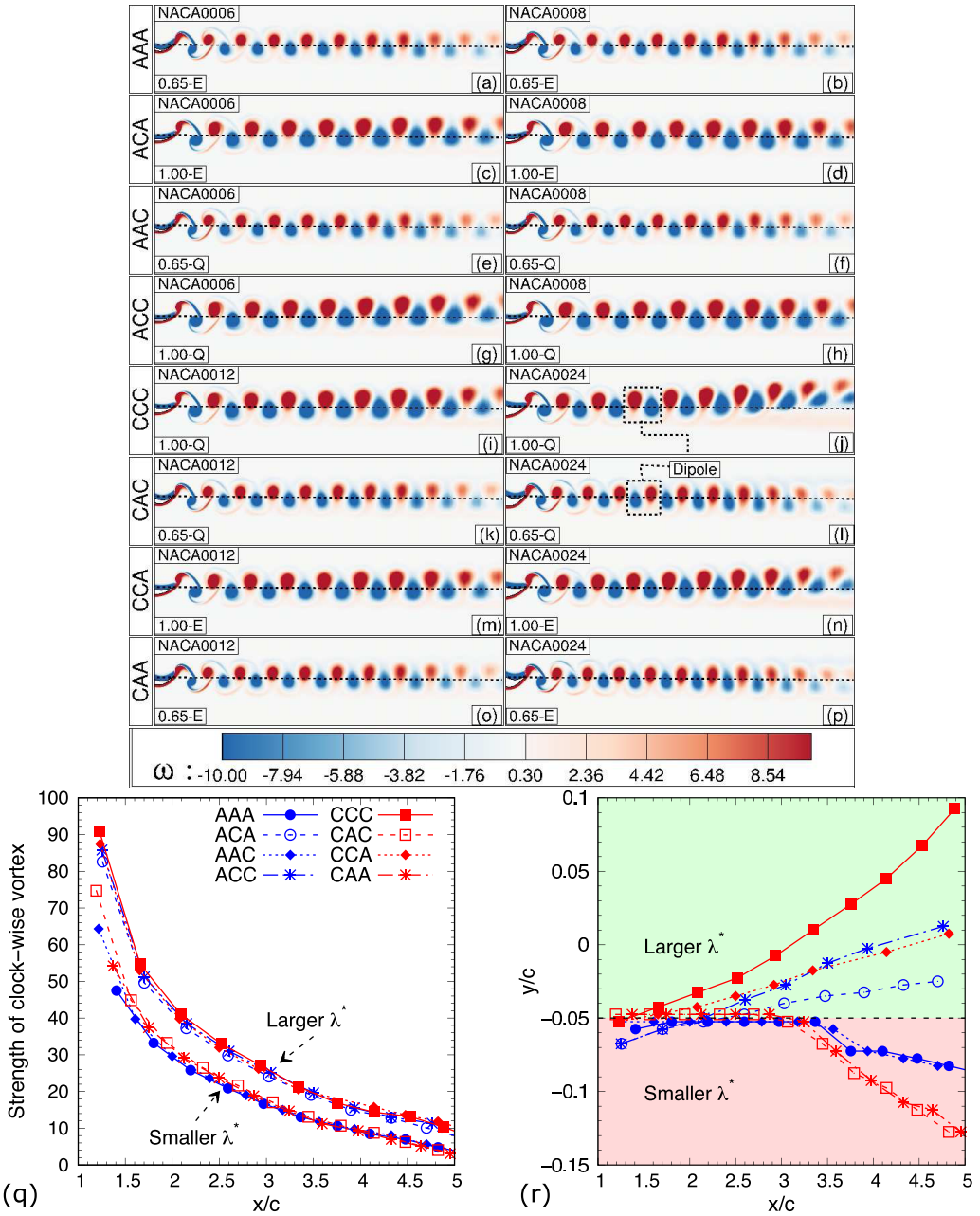

FIG. 9. Variation in the instantaneous vorticity contour behind the hydrofoil and (q, r) streamwise variation of the strength and center of the clockwise shed vortices with the adaptation of each other's λ^*, $A(X)$, and both λ^* and $A(X)$ by various types of anguilliform and carangiform fish-inspired swimming foils, at Re = 5000, St = 0.6, and $A_{\max} = 0.1$. The hydrofoils are shown at their mean position in (a)–(p), and (q) and (r) correspond to NACA0006 and NACA0024 hydrofoil for anguilliform and carangiform shapes, respectively.

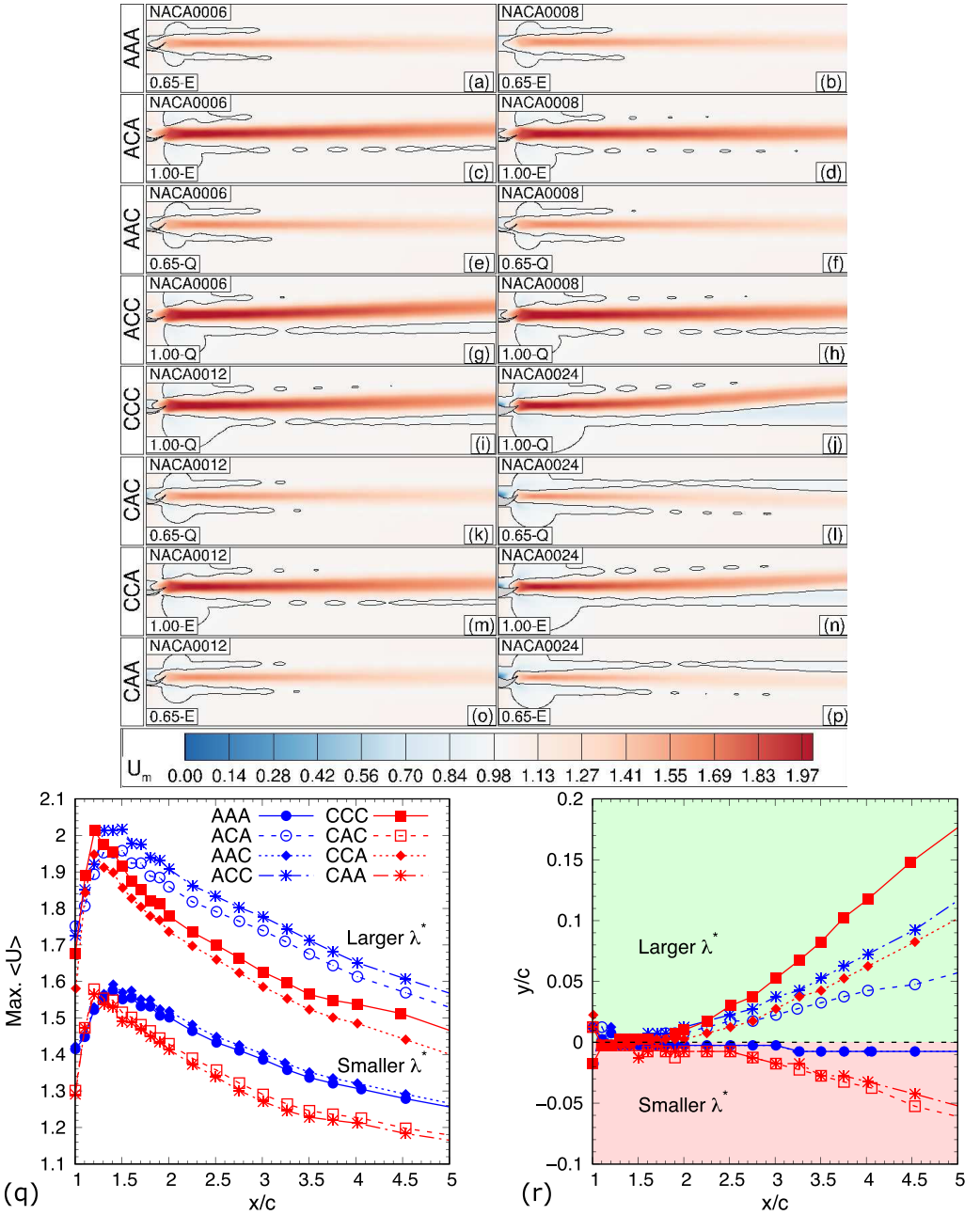

FIG. 10. Variation in the time-averaged streamwise velocity contour behind the hydrofoil and (q, r) streamwise variation of the strength and lateral position of the time-averaged streamwise jet with the adaptation of each other's λ^*, $A(X)$, and both λ^* and $A(X)$ by various types of anguilliform and carangiform fish-inspired swimming foils, at Re $= 5000$, St $= 0.6$, and $A_{\max} = 0.1$. The hydrofoils are shown at their mean position in (a)–(p), and (q) and (r) correspond to NACA0006 and NACA0024 hydrofoils for anguilliform and carangiform shapes, respectively.

asymmetric flow pattern behind the hydrofoil is due to the formation of a dipole within the vortex street. As shown marked in Fig. 9(j), the dipole refers to two opposite-sign vortices that are very close to each other—the closeness is due to the combined effect of vortex stretching and a reduction in the convective velocity of the vortices as they move away from the hydrofoil. Once a vortex is shed from the tail tip, it is convected at a velocity close to the wave speed V_w of undulation. Due to the lower propulsive velocity $u_p < V_w$, the convective velocity reduces downstream; this results in a decrease in the streamwise distance between the upstream and downstream vortices leading to the formation of a dipole. As the dipole forms, the opposite signed vortices induces the surrounding fluid to pass through the narrow gap between the vortex pair (governed by the Biot-Savart law), resulting in an inclined jet [28,34]. The vortices then convect downstream in the direction of this newly formed jet and one can observe an inclined vortex street for the CCC fish-inspired swimming. The direction of the lateral inclination (leftward/rightward) depends on the position of the vortices in the dipole. If the dipole is formed such that the leading vortex within the dipole is clockwise [Fig. 9(j)], then it induces velocity towards the right, resulting in the formation of rightward inclined vortex street; and vice versa [Fig. 9(l)]. The dipole leads to the formation of an inclined jet flow behind the hydrofoil, as shown in Fig. 10 (panels i, j, m, n, and r). The leftward or rightward inclination of the vortex street and the jet depends on the initial condition of the onset of kinematics—the initial leftward (rightward) onset of undulation in our simulation is found to lead to rightward (leftward) inclination of the jet. More details on asymmetric wake and the effect of governing parameters are discussed in our recent work [34].

Figures 9 and 10 also show the effect of adaptation of λ^* and/or $A(X)$-based kinematics on the wake and time-averaged jet formation. For various anguilliform fishlike-shaped hydrofoils, Fig. 9 (panels a, b, c, d, and q) and Fig. 10 (panels a, b, c, d, and q) show an increase in the vortex strength as well as the jet strength by adapting λ^* from 0.65 to 1; compare ACA with AAA in the figures. This results in a larger thrust coefficient C_{Tm} for the ACA as compared to AAA fish-inspired locomotion—refer to Fig. 5(b). Further, Fig. 9 (panels a, b, c, d, and r) and Fig. 10 (panels a, b, c, d, and r) show that the adaptation of the undulation wavelength brings asymmetry in the wake for anguilliform-like swimming; compare ACA with AAA in the figures. The increase in the asymmetry of the wake is due to the increase in the strength of vortices generated by the hydrofoil after adapting carangiform's λ^*, which leads to the formation of dipoles with a larger strength. Thus, the Biot-Savart law based magnitude of lateral induced velocities generated by dipoles for ACA becomes strong enough to deviate the vortices from their mean path of motion. In contrast, for the various carangiform fishlike-shaped hydrofoils, Fig. 9 (panels i, j, k, l, and q) and Fig. 10 (panels i, j, k, l, and q) show that the strength of both the vortex and jet decrease by adapting λ^* from 1 to 0.65; compare CAC with CCC in the figures. The decrease in the strength leads to a decrease in C_{Tm} for CAC as compared to CCC as shown in Fig. 5(b). Further, Fig. 9 (panels i, j, k, l, and r) and Fig. 10 (panels i, j, k, l, and r) show that the asymmetry in the wake reduces for the CAC combination; moreover, the lateral direction of deviation changes from rightward to leftward for carangiform-like swimming by adapting anguilliform's λ^*. The change in direction is a result of the change in the leading vortex of the dipole from CW to CCW [marked in Fig. 9(l)], which is due to the change in the onset movement of the hydrofoil from leftward for the CCC to rightward for the CAC (initial condition in our simulation).

For the only $A(X)$-based adaptive kinematics, Fig. 9 (panels a, b, e, f, i, j, m, n, q, and r) and Fig. 10 (panels a, b, e, f, i, j, m, n, q, and r) show no significant change in vortex strength as well as the jet strength for the adaptive as compared to real fish-inspired swimming—compare AAC with AAA and CCA with CCC. However, the lateral deviation of vortices decreases slightly for carangiform-shaped hydrofoils. This results in no significant change in the thrust coefficient C_{Tm} for the adaptive-$A(X)$ cases [Fig. 6(b)]. For both λ^* and $A(X)$-based adaptive kinematics, Fig. 9 (panels a, b, g, h, i, j, o, p, q, and r) and 10 (panels a, b, g, h, i, j, o, p, q, and r) show an increase (decrease) in vortex strength and jet strength by adapting each other's both λ^* and $A(X)$ for anguilliform (carangiform)-inspired swimming. Thus, the effect is similar to that for only λ^*-based adaptive kinematics on time-averaged engineering parameters, as discussed above in Fig. 7 and Sec. III C.

Figure 10 also shows the effect of shape (FR) on the strength of time-averaged jet in the wake. For same λ^* and $A(X)$, the figure shows a stronger jet for the thinner anguilliform as compared to the thicker carangiform-shaped hydrofoil. Further, the wake deviates more for the carangiform-shaped hydrofoil. Overall, the body shape (FR) and undulation wavelength λ^* are found to be the dominating parameters that influences the strength and symmetry of the wake of a fish-inspired undulating hydrofoil.

C. Vorticity characteristics near the hydrofoil: Secondary or protovortex

Figure 11 shows a clockwise (CW) and counterclockwise (CCW) vortex on the right and left side (refer to Fig. 2 for the sides) of the hydrofoil, respectively. Moreover, at the respective sides of the hydrofoil, thrust generating undulations result in a much smaller opposite-signed vorticity region. This is shown by a zoomed region in the figure as the CW vorticity based secondary or protovortex on the left side that is generated around $x/c = 0.3$ gets advected downstream and merges with the primary shedding vortex of the same sign on the opposite (right) side. Semicircular flow based protovortices are reported in the literature for both the anguilliform [3,6,46–48] and carangiform fish [9], and also for undulating water snakes [51]. It is well established that these vortices are formed due to the pressure suction mechanism (discussed in Sec. IV A) which leads to the formation of semi-circular flows from high to low-pressure zones of the hydrofoil.

For all the cases considered in the study for both anguilliform and carangiform fish-inspired shape hydrofoils, Figs. 11(a)–11(h) show that the first recognizable protovortex is generated at approximately $0.3c$ from the head/snout of the hydrofoil, which is similar to the experimental observation on anguilliform fish by Müller *et al.* [3]. After generation, the vortex travels along with the point of maximum excursion of the hydrofoil, and its strength increases as it advances towards the tail. The convection of the protovortex with increasing strength towards the tail also matches with the literature [3,6,46–48,51]. The convection of the protovortex to the tail tip and its merging with the tail vortex of the same sign is seen for all the cases considered in the study. Thus, the present results support the experimental observation by Tytell and Lauder [6], where they observed merging of a similar signed protovortex and the tail vortex. As discussed above, anguilliform fish are known for changing their kinematics according to their need. We present a similar result for the vortex structure near the hydrofoil. The merging of the same sign proto- and tail vortex represents efficient propulsion, whereas the merging of opposite sign vortices represents better stability during the propulsion.

The streamwise variation of the strength of the clockwise (CW) protovortices is shown in Fig. 11(i) for anguilliform shape and Fig. 11(j) for carangiform shape, respectively. Here the strength corresponds to the local maximum of the magnitude of instantaneous vorticity that is found at the center of the CW protovortices. Further, the position of the center of CW protovortices is measured from the head/snout of the hydrofoil. Figures 11(i) and 11(j) also show that the adaptation of undulation wavelength does not have a significant effect on the strength of protovortices; compare ACA with AAA and CAC with CCC. In contrast, with the adaptation of $A(X)$, the strength at any chordwise position decreases for anguilliform (compare AAC with AAA) and increases for carangiform-shaped hydrofoils (compare CCA with CCC). From curve fitting to the data, it is observed that the increase in strength along the chord length is exponential for anguilliform's amplitude envelope (AAA, ACA, CCA, CAA), while the variation is quadratic for cases with carangiform's amplitude envelope (AAC, ACC, CCC, CAC). Thus, one can conclude that for a particular shape, the strength of protovortices depends only on the amplitude envelope $A(X)$ and is independent of the λ^* of undulations.

V. SUMMARY AND CONCLUSIONS

In this section, the 2D CFD results are summarized to explain some of the observed behaviors of a fish in nature. Note that the summary is based only on the hydrodynamic characteristics and

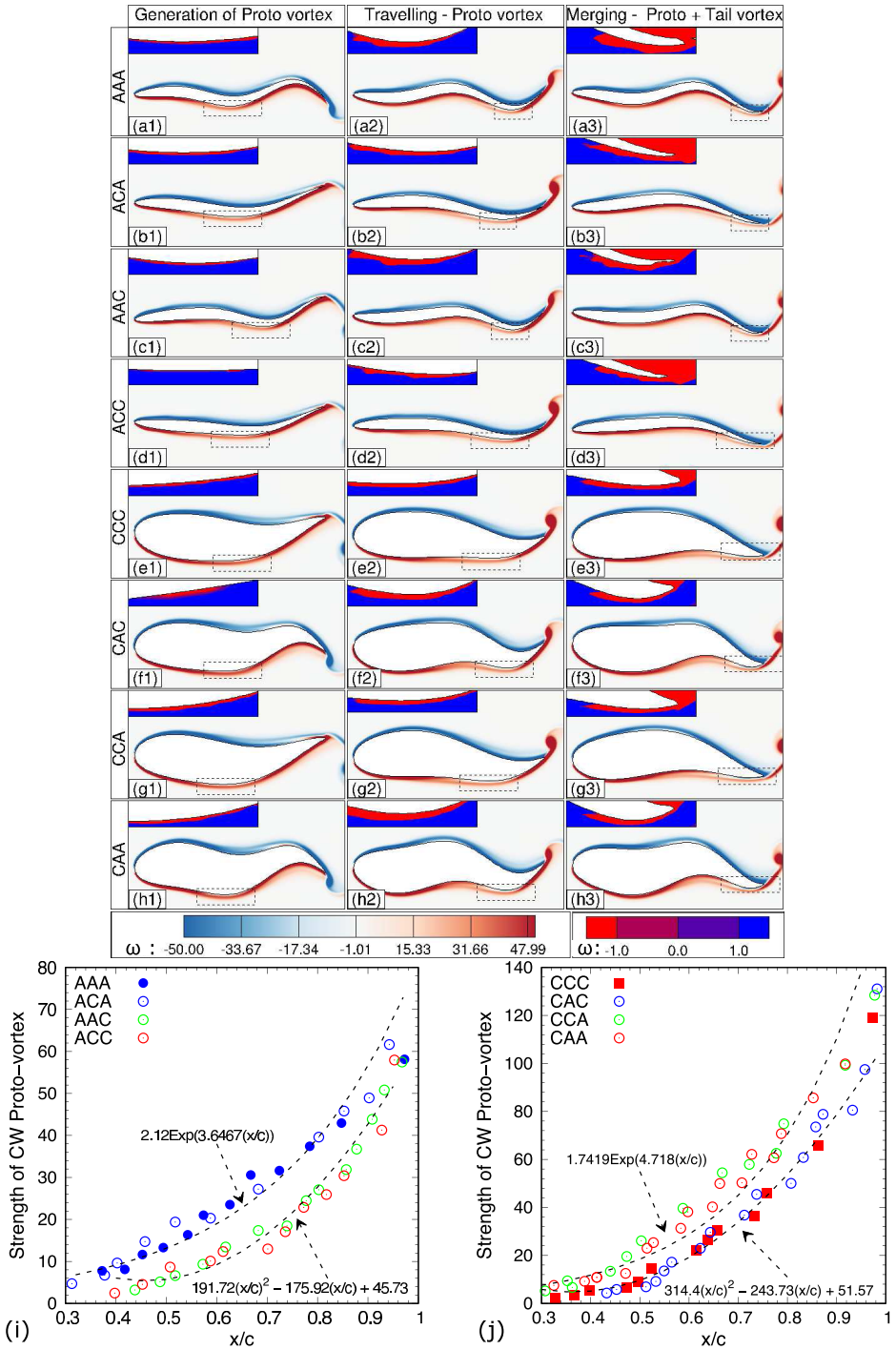

FIG. 11. For the naturally observed and adaptive cases of the anguilliform and carangiform fish-inspired swimming, (a–h) temporal variation of the vorticity contour near the hydrofoil and (i–j) streamwise variation (from the leading edge) of the strength of the clockwise (CW) protovortex. A zoomed view of the dashed rectangular region in the vorticity contours shows the generation, downstream advection, and merging of the protovortex.

propulsive performance of swimming, which may not be complete and sufficient in many cases since evolutionary forces may be influenced by other factors.

In nature, both anguilliform and the carangiform fish have evolved over millions of years to conserve energy or maximize their propulsive efficiency according to their needs. Interestingly, predictions from our simplified numerical simulations are in agreement with the optimal combination of the body shape and undulation pattern, observed in nature, for achieving desired goals. Anguilliform fish possess an elongated/thinner body, swim at slow to moderate velocity, and have habitats in the benthic zone (close to the lowest level) of the water body [52]. Due to this slow to moderate swimming speed, they do not require high thrust; however, they do need to save their energy due to the structurally complex environment at the bed of the water body. Hence, they have developed their undulation kinematics such that they can swim at high efficiency. In contrast, carangiform fish possess comparatively thicker/fusiform bodies, are moderate to very fast swimmers, and have habitats in the pelagic zone (neither close to the bed nor near the surface) of the water body [52]. Thus, they need to generate larger velocities or larger thrust but still should be reasonably efficient. Hence, they have developed their undulation kinematics such that they can swim at high speeds, while still maintaining reasonable efficiencies consistent with their body shape.

Our simulation results show that for an anguilliform fish-inspired hydrofoil, the adaptation of undulation wavelength λ^* provides a larger thrust generation that results in enhanced acceleration while reducing quasipropulsive efficiency η_{QP} (Sec. III A). In nature, this is exemplified in needlefish (anguilliform fish and also known as flying fish) undulating at a larger wavelength close to that of carangiform fish, since they require a large acceleration to jump to jump out of the water [2]. In contrast to anguilliform fish-inspired undulating hydrofoils, the present result for carangiform fish-inspired undulating hydrofoils show that the adaptation of the undulation wavelength λ^* causes a reduction in thrust generation. However, quasipropulsive efficiency η_{QP} increases significantly.

Nature seems to have a very effective and simple strategy to optimize propulsive performance. Carangiform fish possess comparatively thicker bodies, undulate with a quadratic amplitude envelope and a larger undulation wavelength. Our simulations show that these combinations provide a large magnitude of C_{Lrms}, which reduces the lateral stability during locomotion. However, carangiform fish are equipped with additional paired fins to stabilize themselves under the effect of larger lateral forces [53,54]. On the other hand, thin and elongated anguilliform fish undulate with an exponential envelope and smaller undulation wavelength. The present results show that the anguilliform body shape and kinematics generates smaller lateral forces that allow reasonable stability without fins.

In terms of the vortical flow structure created behind the anguilliform and carangiform fish-inspired swimming, the present results show that the strength and symmetry of the wake depends on the undulation wavelength and body shape (FR). Thus, the wake from anguilliform fish-inspired swimming is of low strength and dissipates quickly as compared to carangiform fish-inspired swimming (Sec. IV B). This low strength and quickly dissipating vortical structure is associated with the survival of anguilliform fish against most predator fish (mostly large fish that come under the category of carangiform and thunniform) and cetaceans. Predator fish generally possess mechano-sensitive organs that use vortices that are left behind in the wake as signals to locate the position of prey [55–58]. Thus, to escape detection of predators, anguilliform fish endeavour to shed smaller vortices.

The conclusions drawn from the present study are as follows:

(1) By adapting the undulation wavelength λ^* of carangiform (anguilliform) fish, the mean thrust generation for anguilliform (carangiform) fish-inspired-shaped hydrofoils increases (decreases); however, this adaptation reduces (increases) the stability and quasipropulsive efficiency of swimming. The variation in the propulsive performance is supported by the flow field as the magnitude of vortex strength and jet strength increases (decreases) in the wake; and the adaptation brings (reduces) asymmetry in the convection of vortices and the jet.

(2) By adapting the amplitude envelope of a carangiform (anguilliform) fish, there is no significant change in the mean thrust generation and quasipropulsive efficiency for anguilliform

fish-inspired-shaped hydrofoils; however, this adaptation reduces the stability of swimming considerably. In contrast, for carangiform fish-inspired-shaped hydrofoils, the quasipropulsive efficiency and stability of swimming enhances.

(3) The effect of adaptation of both λ^* and $A(X)$ on the propulsive performance parameters is almost the same as with the adaptation of λ^* only.

(4) For the flow structure, the strength and symmetry of vortices in the wake are more strongly influenced by the undulating wavelength λ^* as compared to the amplitude envelope $A(X)$, while the flow field in the vicinity of the hydrofoil (protovortex) is found to be associated with $A(X)$.

The above conclusions, although based on simplified 2D-model-based results, presents a reasonable justification of various types of adaptive swimming characteristics of anguilliform and carangiform fish. For the role and relation between body-shape, undulation-wavelength, and amplitude-envelope on the propulsive performance, although the present results provide a 2D flow characteristic-based hydrodynamic analysis, 3D flow characteristics can lead to more realistic reasoning and will be attempted in a future study. A novel contribution of the present study is the mapping of different shapes of fish body with appropriate shapes of NACA hydrofoils that can be beneficial to future investigations on fish-inspired swimming. One of the important contributions of the reported results is that it can be used for a need based designing of autonomous underwater vehicles.

ACKNOWLEDGMENT

S.G. acknowledges the continuous help and support received from Dr. Namshad Thekkethil (IIT Bombay) on using the in-house code for the present problem.

[1] N. Nangia, R. Bale, N. Chen, Y. Hanna, and N. A. Patankar, Optimal specific wavelength for maximum thrust production in undulatory propulsion, PLoS ONE **12**, e0179727 (2017).

[2] J. C. Liao, Swimming in needlefish (Belonidae): Anguilliform locomotion with fins, J. Exp. Biol. **205**, 2875 (2002).

[3] U. K. Müller, J. Smit, E. J. Stamhuis, and J. J. Videler, How the body contributes to the wake in undulatory fish swimming: Flow fields of a swimming eel (*Anguilla anguilla*), J. Exp. Biol. **204**, 2751 (2001).

[4] J. M. Donley and R. E. Shadwick, Steady swimming muscle dynamics in the leopard shark Triakis semifasciata, J. Exp. Biol. **206**, 1117 (2003).

[5] J. Videler, Swimming movements, body structure and propulsion in cod Gadus morhua, Symp. Zool. Soc. Lond. **48**, 1 (1981).

[6] E. D. Tytell and G. V. Lauder, The hydrodynamics of eel swimming: I. Wake structure, J. Exp. Biol. **207**, 1825 (2004).

[7] J. Videler and F. Hess, Fast continuous swimming of two pelagic predators, saithe (*Pollachius virens*) and mackerel (*Scomber scombrus*): A kinematic analysis, J. Exp. Biol. **109**, 209 (1984).

[8] J. C. Breder, The locomotion of fishes, Zoologica **4**, 159 (1926).

[9] U. Müller, B. Van Den Heuvel, E. Stamhuis, and J. Videler, Fish foot prints: Morphology and energetics of the wake behind a continuously swimming mullet (*Chelon labrosus risso*), J. Exp. Biol. **200**, 2893 (1997).

[10] M. Hultmark, M. Leftwich, and A. J. Smits, Flowfield measurements in the wake of a robotic lamprey, Exp. Fluids **43**, 683 (2007).

[11] M. Leftwich and A. Smits, Thrust production by a mechanical swimming lamprey, Exp. Fluids **50**, 1349 (2011).

[12] G.-J. Dong and X.-Y. Lu, Characteristics of flow over traveling wavy foils in a side-by-side arrangement, Phys. Fluids **19**, 057107 (2007).

[13] Y. Sui, Y.-T. Chew, P. Roy, and H.-T. Low, A hybrid immersed-boundary and multi-block lattice Boltz-

mann method for simulating fluid and moving-boundaries interactions, Int. J. Numer. Methods Fluids **53**, 1727 (2007).
[14] X. Shao, D. Pan, J. Deng, and Z. Yu, Hydrodynamic performance of a fishlike undulating foil in the wake of a cylinder, Phys. Fluids **22**, 111903 (2010).
[15] N. Thekkethil, A. Sharma, and A. Agrawal, Unified hydrodynamics study for various types of fishes-like undulating rigid hydrofoil in a free stream flow, Phys. Fluids **30**, 077107 (2018).
[16] M. S. U. Khalid, J. Wang, H. Dong, and M. Liu, Flow transitions and mapping for undulating swimmers, Phys. Rev. Fluids **5**, 063104 (2020).
[17] S. Kern and P. Koumoutsakos, Simulations of optimized anguilliform swimming, J. Exp. Biol. **209**, 4841 (2006).
[18] I. Borazjani and F. Sotiropoulos, Numerical investigation of the hydrodynamics of anguilliform swimming in the transitional and inertial flow regimes, J. Exp. Biol. **212**, 576 (2009).
[19] I. Borazjani and F. Sotiropoulos, Numerical investigation of the hydrodynamics of carangiform swimming in the transitional and inertial flow regimes, J. Exp. Biol. **211**, 1541 (2008).
[20] I. Borazjani and F. Sotiropoulos, On the role of form and kinematics on the hydrodynamics of self-propelled body/caudal fin swimming, J. Exp. Biol. **213**, 89 (2010).
[21] W. M. Van Rees, M. Gazzola, and P. Koumoutsakos, Optimal shapes for anguilliform swimmers at intermediate Reynolds numbers, J. Fluid Mech. **722**, R3 (2013).
[22] W. M. Van Rees, M. Gazzola, and P. Koumoutsakos, Optimal morphokinematics for undulatory swimmers at intermediate Reynolds numbers, J. Fluid Mech. **775**, 178 (2015).
[23] M. J. McHenry and G. V. Lauder, Ontogeny of form and function: Locomotor morphology and drag in zebrafish (*Danio rerio*), J. Morphol. **267**, 1099 (2006).
[24] R. Bainbridge, Speed and stamina in three fish, J. Exp. Biol. **37**, 129 (1960).
[25] R. Blake, Functional design and burst-and-coast swimming in fishes, Can. J. Zool. **61**, 2491 (1983).
[26] J. L. Lim and G. V. Lauder, Mechanisms of anguilliform locomotion in fishes studied using simple three-dimensional physical models, Bioinspir. Biomim. **11**, 046006 (2016).
[27] A. Maertens, M. S. Triantafyllou, and D. K. Yue, Efficiency of fish propulsion, Bioinspir. Biomim. **10**, 046013 (2015).
[28] N. Thekkethil, A. Sharma, and A. Agrawal, Self-propulsion of fishes-like undulating hydrofoil: A unified kinematics based unsteady hydrodynamics study, J. Fluids Struct. **93**, 102875 (2020).
[29] Z. Cui, X. Gu, K. Li, and H. Jiang, CFD studies of the effects of waveform on swimming performance of carangiform fish, Appl. Sci. **7**, 149 (2017).
[30] A. P. Maertens, A. Gao, and M. S. Triantafyllou, Optimal undulatory swimming for a single fish-like body and for a pair of interacting swimmers, J. Fluid Mech. **813**, 301 (2017).
[31] A. Gao and M. S. Triantafyllou, Independent caudal fin actuation enables high energy extraction and control in two-dimensional fish-like group swimming, J. Fluid Mech. **850**, 304 (2018).
[32] N. Wagenhoffer, K. W. Moored, and J. W. Jaworski, Unsteady propulsion and the acoustic signature of undulatory swimmers in and out of ground effect, Phys. Rev. Fluids **6**, 033101 (2021).
[33] S. Gupta, N. Thekkethil, A. Agrawal, K. Hourigan, M. C. Thompson, and A. Sharma, Body-caudal fin fish-inspired self-propulsion study on burst-and-coast and continuous swimming of a hydrofoil model, Phys. Fluids **33**, 091905 (2021).
[34] S. Gupta, A. Sharma, A. Agrawal, M. C. Thompson, and K. Hourigan, Hydrodynamics of a fish-like body undulation mechanism: Scaling laws and regimes for vortex wake modes, Phys. Fluids **33**, 101904 (2021).
[35] H. Liu, R. Wassersug, and K. Kawachi, The three-dimensional hydrodynamics of tadpole locomotion, J. Exp. Biol. **200**, 2807 (1997).
[36] H. Liu, R. Wassersug, and K. Kawachi, A computational fluid dynamics study of tadpole swimming, J. Exp. Biol. **199**, 1245 (1996).
[37] M. Gazzola, W. M. Van Rees, and P. Koumoutsakos, C-start: Optimal start of larval fish, J. Fluid Mech. **698**, 5 (2012).
[38] U. K. Muller, J. G. van den Boogaart, and J. L. van Leeuwen, Flow patterns of larval fish: Undulatory swimming in the intermediate flow regime, J. Exp. Biol. **211**, 196 (2008).

[39] A. Zurman-Nasution, B. Ganapathisubramani, and G. Weymouth, Influence of three-dimensionality on propulsive flapping, J. Fluid Mech. **886**, A25 (2020).
[40] N. Thekkethil and A. Sharma, Level set function–based immersed interface method and benchmark solutions for fluid flexible-structure interaction, Int. J. Numer. Methods Fluids **91**, 134 (2019).
[41] N. Thekkethil, A. Sharma, and A. Agrawal, Three-dimensional biological hydrodynamics study on various types of batoid fishlike locomotion, Phys. Rev. Fluids **5**, 023101 (2020).
[42] T. Van Buren, D. Floryan, A. T. Bode-Oke, P. Han, H. Dong, and A. Smits, Foil shapes for efficient fish-like propulsion, in *AIAA Scitech 2019 Forum* (2019), p. 1379.
[43] A. Sharma, *Introduction to Computational Fluid Dynamics: Development, Application and Analysis* (John Wiley & Sons, New York, 2016).
[44] R. Blickhan, C. Krick, D. Zehren, W. Nachtigall, and T. Breithaupt, Generation of a vortex chain in the wake of a suhundulatory swimmer, Naturwissenschaften **79**, 220 (1992).
[45] R. Bale, I. D. Neveln, A. P. S. Bhalla, M. A. MacIver, and N. A. Patankar, Convergent evolution of mechanically optimal locomotion in aquatic invertebrates and vertebrates, PLoS Biol. **13**, e1002123 (2015).
[46] J. Gray, *Animal Locomotion* (Weidenfeld and Nicholson, London, 1968).
[47] B. J. Gemmell, S. M. Fogerson, J. H. Costello, J. R. Morgan, J. O. Dabiri, and S. P. Colin, How the bending kinematics of swimming lampreys build negative pressure fields for suction thrust, J. Exp. Biol. **219**, 3884 (2016).
[48] J. Videler, U. Muller, and E. Stamhuis, Aquatic vertebrate locomotion: Wakes from body waves, J. Exp. Biol. **202**, 3423 (1999).
[49] M. Wolfgang, J. Anderson, M. Grosenbaugh, D. Yue, and M. Triantafyllou, Near-body flow dynamics in swimming fish, J. Exp. Biol. **202**, 2303 (1999).
[50] J. C. Nauen and G. V. Lauder, Hydrodynamics of caudal fin locomotion by chub mackerel, *Scomber japonicus* (Scombridae), J. Exp. Biol. **205**, 1709 (2002).
[51] H. Hertel, *Structure, Form, Movement* (Reinhold, New York, 1966).
[52] G. S. Helfman, B. B. Collette, and D. E. Facey, *The Diversity of Fishes* (Blackwell Science, Malden, MA, 1997).
[53] E. G. Drucker and G. V. Lauder, Locomotor forces on a swimming fish: Three-dimensional vortex wake dynamics quantified using digital particle image velocimetry, J. Exp. Biol. **202**, 2393 (1999).
[54] F. Fish and G. V. Lauder, Passive and active flow control by swimming fishes and mammals, Annu. Rev. Fluid Mech. **38**, 193 (2006).
[55] S. Dijkgraaf, The functioning and significance of the lateral-line organs, Biol. Rev. **38**, 51 (1963).
[56] H. Bleckmann, Role of the lateral line in fish behaviour, in *The Behaviour of Teleost Fishes*, edited by T. J. Pitcher (Springer, Boston, MA, 1986), pp. 177–202.
[57] S. Coombs and J. C. Montgomery, The enigmatic lateral line system, in *Comparative Hearing: Fish and Amphibians*, edited by R. R. Fay and A. N. Popper, Springer Handbook of Auditory Research Vol. 11 (Springer, New York, NY, 1999), pp. 319–362.
[58] S. M. van Netten, Hydrodynamic detection by cupulae in a lateral line canal: Functional relations between physics and physiology, Biol. Cybern. **94**, 67 (2006).